

Clean room at the department Silicon Photovoltaics

A scientist wearing a white lab coat and safety goggles is working in a laboratory. The background shows laboratory equipment and a desk with a chair.

Scientific Highlights Solar Energy Research 2006

SE1 Silicon Photovoltaics	60
SE2 Heterogeneous Material Systems	66
SE3 Technology	68
SE4 Dynamics of Interfacial Reactions	72
SE5 Solar Energetics	78
SE6 Electronic Structure of Semiconductor Interfaces	88

Electronic states in *a*-Si:H/*c*-Si heterostructures

L. Korte, A. Laades, M. Schmidt

■ HMI, SE 1

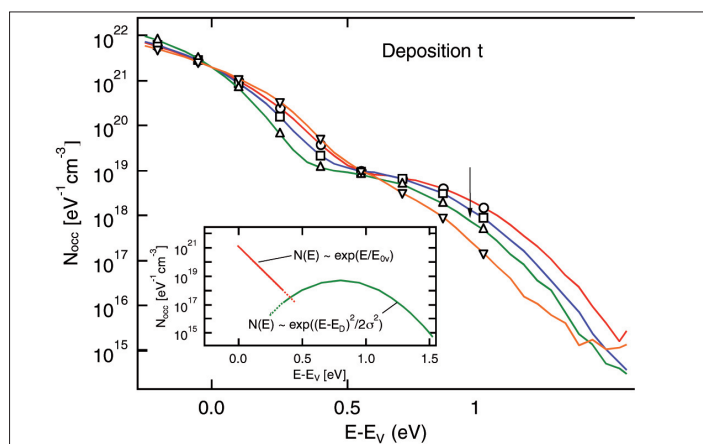


Fig. 1: Density of occupied gap states $N_{\text{occ}}(E)$ of a series of *a*-Si:H(i)/*c*-Si(p) samples with variation of the *a*-Si:H deposition temperature T_s . E_v is the origin of the abscissa. Arrows mark the Fermi level positions. The spectra are normalized to $2 \cdot 10^{21}$ states/(eV·cm³) at the valence band edge. Inset: Decomposition of the DOS into Urbach tail and dangling bond distribution (schematic).

Introduction

The key to obtaining high cell efficiencies of amorphous-crystalline (*a*-Si:H/*c*-Si) heterojunction solar cells with monocrystalline or polycrystalline silicon absorbers is the quality of the *p/n* heterojunction formed by the deposition of *a*-Si:H emitter. The use of heterostructures for the realisation of *p/n* junctions requires a careful analysis of electronic states in the involved solids and at their hetero-interface.

The main parameters determining charge transfer and recombination activity are the band offsets and the Fermi level position at the *a*-Si:H/*c*-Si interface as well as the density and energetic distribution of defect states (DOS) at the interface and in the thin amorphous layer. Little is known about the electrical properties of ultra-thin films and their interfaces. In recent years, we have developed experimental techniques that are especially well-suited to the characterisation of such films and their interface to the substrate [1,2,3].

Sample Preparation

All investigated *a*-Si:H layers, with thicknesses of 12 to 17 nm, were deposited on <111> oriented silicon

by RF excited PECVD (13.6 MHz, $P_{\text{RF}} = 13$ mW/cm²) using silane, SiH₄, as precursor. Prior to *a*-Si:H deposition, all wafers were cleaned (standard RCA-procedure), followed by an HF dip (1% HF, 1 minute) and immediate transfer into the PECVD system.

Constant Final State Photoelectron Spectroscopy

The *a*-Si:H density of states (DOS) was obtained using photoelectron spectroscopy in the so-called constant final state yield spectroscopy mode (CFSYS) [4,5]. Here, instead of the photoelectron analyser energy, the energy of the exciting photons is varied. This has the advantage that for all points in the spectrum (photoelectron yield γ_{int} vs. photon energy $h\nu$), photoelectrons excited into the same conduction band state(s) – final states – are measured. Thus, details of the conduction band structure have no influence on the shape of the spectrum. In general, this technique is only available at tuneable photon sources such as synchrotrons; our set-up provides the same functionality – albeit at a very limited photon energy range of $h\nu = 3 - 7$ eV – in a conventional UPS/XPS laboratory system. From the measured spectra, the po-

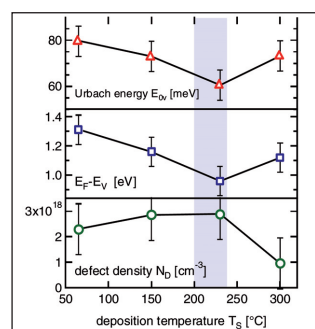
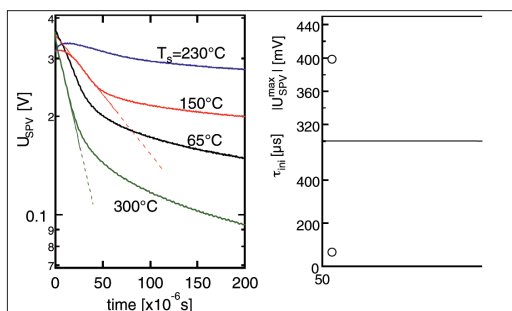


Fig. 2: Data derived from the series shown in Fig. 1: Dependence on T_s of (i) Urbach energy E_0 , (ii) Fermi level position $E_F - E_v$ and (iii) integrated defect density N_D .

sition of the Fermi level E_F , of the valence band edge E_v and the distribution of occupied states $N_{\text{occ}}(E)$ normalised to units of [states/(cm³eV)] are obtained. The measured distribution is a weighted average of the DOS of the sample up to a depth of 7 to 10 nm. For further details see [1,2,5].

Surface Photovoltage

To determine the band bending in the *c*-Si and a characteristic time constant for recombination at the *a*-Si:H/*c*-Si interface, surface photovoltage



(SPV) [6,7,8] measurements were used. Upon intense illumination of the sample by a laser pulse ($h\nu = 1.35$ eV, pulse duration 160 ns, intensity 10^{19} photons/(cm²s)), excess charge carriers are generated, leading to a flattening of the bands and a split-up of the quasi Fermi levels of electrons and holes. The surface photovoltage of the sample is then measured capacitively as photovoltage pulse U_{SPV} . Because the sample is illuminated at a photon energy smaller than the band gap of *a*-Si:H (~ 1.7 eV), the latter acts as a window layer, the excitation of charge carriers takes place in the crystalline substrate. Their recombination can be characterised via the time dependent U_{SPV} decay.

Results

The density of occupied states $N_{occ}(E)$ is shown in Fig. 1. The usual features, i.e. an exponential decay of the DOS at $E - E_V = 0 \dots \sim 0.4$ eV and a Gaussian-shaped defect distribution up to E_F are observed. Fig. 2 shows parameters derived from Fig. 1: The Urbach energy E_{0v} , E_F and the integrated defect density of deep defects N_D vs. substrate temperature T_S during *a*-Si:H deposition. Both Urbach energy and E_F depend on deposition temperature and have a minimum at $T_S = 230^\circ\text{C}$. In contrast, N_D shows, within the accuracy of the measurement, no appreciable variation and is slightly higher than the value of $8 \cdot 10^{17}$ cm⁻³ reported for thick films. The shift of E_F correlates with a shift of the deep defect (Fig. 1). The corresponding SPV transients are presented in Fig. 3. The decay of the transient is an image of the recombination of photo-generated excess carriers that occurs predominantly at the *a*-Si:H/*c*-Si interface. The first ~ 50 μs of the decay are exponential, described by a time constant τ_{ini} that has a pronounced maximum at $T_S \sim 200 - 230^\circ\text{C}$. The minimum of the initial photovoltage U_{SPV}^{max} lies at the same deposition temperature. As shown in [3], photoluminescence and the efficiency of solar cells processed with *n*-doped emitters prepared under identical conditions have a maximum at the same T_S .

In ref. [2], we calculate the Fermi level at the *a*-Si:H/*c*-Si interface. We find that E_F crosses the interface at only 45 meV above midgap. In Shockley-Read-Hall recombination statistics, the effective recombination velocity increases when E_F approaches midgap. However, the measured τ_{ini} is

Fig. 3: Left: Surface photovoltage transients measured on the deposition temperature series shown in Fig. 1. For $T_S = 150$ and 300°C , exponential fits to obtain τ_{ini} are plotted. Right: Dependence of the maximum photovoltage [U_{SPV}^{max}] and the slope parameter of the initial fast decay τ_{ini} on T_S . \circ : for the series of Fig. 1, \square : for an additional series deposited under the same conditions. Lines are guides to the eye.

highest for E_F at the interface closest to midgap. Thus, the interface state density, which is assumed to be predominantly related to Si dangling bonds with back-bonds to the *c*-Si substrate, must be reduced after the deposition of *a*-Si:H under optimised conditions. Deposition under sub-optimal conditions, however, leads to an increase of the density of localised states in the gap, but close

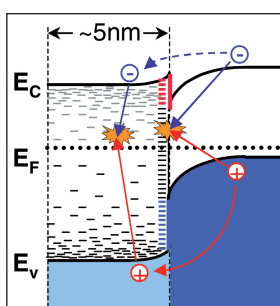


Fig. 4: Schematic band diagram of the *a*-Si:H/*c*-Si interface, arrows show the proposed tunneling and recombination paths.

to the band edges (E_{0v} is increased). This causes enhanced recombination, which can be attributed to tunnel hopping of charge carriers into *a*-Si:H tail states and subsequent recombination via *a*-Si:H gap states (Fig. 4), as shown by EDMR measurements [9].

- [1] M. Schmidt, A. Schoepke, L. Korte, O. Milch, W. Fuhs, J. Non-Cryst. Sol. **338-340** (2004) 211.
- [2] L. Korte, A. Laades, M. Schmidt, J. Non-Cryst. Sol. **352** (2006) 1217.
- [3] K. v. Maydell, L. Korte, A. Laades, R. Stangl, E. Conrad, F. Lange, M. Schmidt, J Non-Cryst. Sol. **352** (2006) 1958.
- [4] M. Sebastiani, L. D. Gaspare, G. Capellini, C. Bittencourt, F. Evangelisti, Phys. Rev. Lett. **75** (1995) 3352.
- [5] L. Korte, PhD thesis, U Marburg / Hahn-Meitner-Institut Berlin, 2006 (HMI-Bericht Nr. 611, ISSN 0936-0891).
- [6] A. Laades, PhD thesis, TU Berlin / Hahn-Meitner-Institut Berlin, 2005 (ISBN 978-3-86664 078-8).
- [7] Y. Lam, J. Phys. D: Appl. Phys. **4** (1971) 1370.
- [8] W. Füssel, M. Schmidt, H. Angermann, G. Mende, H. Flietner, Nucl. Instrum. Meth. Phys. Res. B **377** (1996) 177.
- [9] C. Boehme, J. Behrend, K.v. Maydell, M. Schmidt, K. Lips, J. Non-Cryst. Sol. **352** (2006) 1113.

Corresponding author:

M. Schmidt
schmidt-m@hmi.de

Optical quenching of hydrogen donor states in zinc oxide

N. H. Nickel

■ HMI, SE 1

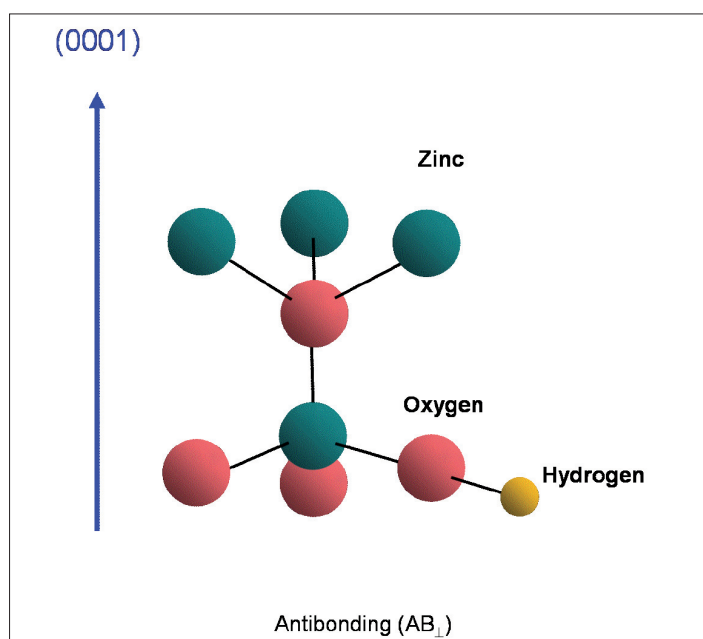


Fig. 1: Schematic depiction of the hydrogen shallow donor complexes in zinc oxide.

To fabricate fully transparent optoelectronic devices it is essential to grow *n*-type and *p*-type wide band-gap semiconductors. One of the materials of choice is ZnO. However, one of the major drawbacks is the fact that most available ZnO bulk crystals and thin films exhibit *n*-type conductivity. Interestingly, the unique properties of hydrogen in semiconductors have been identified as one of the major problems hindering *p*-type doping of ZnO [1,2]. Recently, the microscopic structure of H shallow donors was identified as O-H donor complexes in the antibonding configuration AB_⊥ with a characteristic vibrational frequency of 3326.4 cm⁻¹ [3]. The microscopic structure of this donor complex is schematically depicted in Fig. 1.

Post-hydrogenation of ZnO single crystals was achieved using ampoule hydrogenation. Then the samples were characterized with Fourier transform infrared spectroscopy using an instrumental resolution of 0.5 to 1.0 cm⁻¹. All mea-

surements and light soaking were performed at 5 K. For light soaking a high efficiency LED was used that emitted blue light with a wave length of $\lambda = 450$ nm.

IR spectra of hydrogenated ZnO single crystals are shown in Fig. 2. Hydrogenation produces a strong local vibrational mode at $\nu = 3326.6$ cm⁻¹ (Fig. 2(a)) that is due to the formation of O-H donor complexes where the hydrogen atom resides at the anti-bonding site [3]. Prior to the illumination the IR line associated with the H shallow donor shows the largest intensity. Then the ZnO sample was illuminated at 5 K for 2 min and the O-H absorption line was measured again. The intensity of the O-H vibrational mode decreased upon illumination (Fig. 2(b)). The quenching of the O-H infrared absorption line due to sub band-gap illumination is completely reversible. When the specimen was annealed at 100 K for 5 min the O-H absorption line recovered completely (Fig. 2 (c)).

The annealing behavior of the quenched O-H vibrational line was investigated in more detail. For this purpose a hydrogenated ZnO specimen was illuminated with blue light until the infrared signal was minimized. Then, the sample was heated to the desired temperature where it was annealed for 5 min. Subsequently the ZnO crystal was cooled to 5 K and the O-H absorption line was measured again. In Fig. 3 the change of the integrated O-H intensity, ΔI_{OH} , due to isochronal annealing is plotted as a function of the annealing temperature, T_A . With increasing annealing temperature ΔI_{OH} reaches a maximum at 45 K and then decreases to a value below zero at $T_A = 70$ K. At higher annealing temperatures ΔI_{OH} exhibits a pronounced increase and eventually saturates at $T_A \geq 100$ K indicating that the intensity of the O-H vibrational line was completely recovered.

The temperatures at which quenching and recovery of the O-H absorption line occurs suggest that the underlying process is governed by charge carriers. Without changing the number of O-H complexes an increase or decrease of the infrared absorption line can only occur when the dipole moment, p , and hence, the infrared effective charge e^* changes ($p \propto e^*$).

From the integral of the O-H absorption line, which amounts to 5.934 cm^{-1} , the effective charge of the O-H dipole can be estimated [4]. Assuming that all H atoms form ionized O-H⁺ complexes an effective charge of the O-H⁺ complex of $e^* = 0.135 e$ was obtained. Since the number of H atoms accommodated in O-H⁺ complexes might be lower than the total H concentration the calculated value for e^* denotes a lower limit.

When the sample is illuminated photo generated electrons are trapped in the O-H complex, which lowers the concentration of O-H⁺ centers. This should result in the appearance of an additional vibrational mode due to O-H⁰ complexes. However, an additional line due to the change of the dipole moment was not observed. This suggests that the dipole moment of the O-H⁰ complex is too small to permit the observation of a vibrational mode by IR absorption.

The decrease of ΔI_{OH} between $T_A = 50$ and 75 K is unexpected and indicates that the underlying mechanism is more complex than the

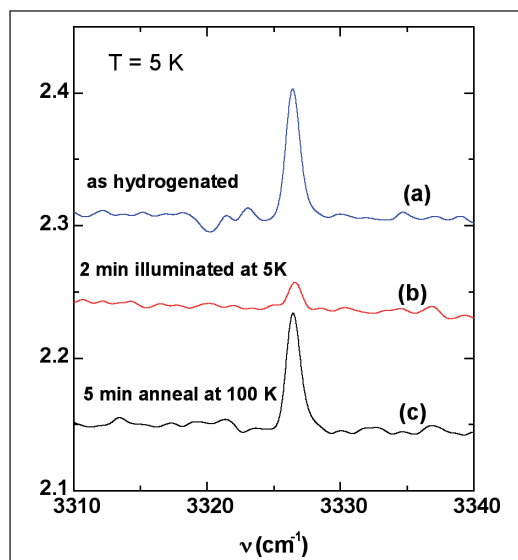


Fig. 2: IR absorption spectra of hydrogenated ZnO single crystals measured at $T=5 \text{ K}$. (a) after hydrogenation, (b) after illumination at 5 K for 2 min , and (c) after a subsequent anneal at 100 K for 5 min .

simple ionization of neutral O-H complexes. A decrease of ΔI_{OH} can only occur when electrons are captured by O-H⁺ complexes. Since the annealing experiments were performed at low temperatures the capture of free electrons is unlikely. However, defect states that reside deeper in energy at E_D (see sketch in Fig. 3) can act as an efficient source of electrons.

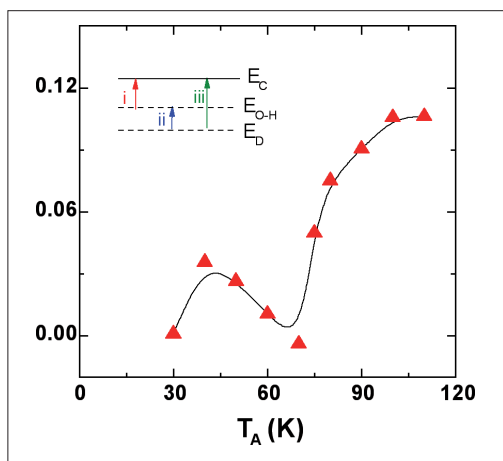


Fig. 3: Change of the integrated O-H vibrational line, ΔI_{OH} , as a function of the annealing temperature, T_A . Prior to each anneal the sample was illuminated with light from a blue LED. All spectra were measured at 5 K .

During illumination these defect states also have captured electrons. With increasing T_A electrons trapped at E_D are thermally excited and recaptured by O-H⁺ complexes (process ii in Fig. 3). For the experimental conditions chosen this results in a pronounced decrease of ΔI_{OH} for annealing temperatures between 50 and 75 K . Eventually as T_A increases further, electrons from E_D can also be excited into the conduction band (iii in Fig. 3). Consequently ΔI_{OH} increases rapidly.

In summary, we have shown that infrared absorption of the O-H vibrational line is very sensitive to sub band-gap illumination. Illumination at liquid-helium temperatures results in a pronounced decrease of the O-H absorption line. This effect is completely reversible by annealing the specimens at temperatures above $T_A=30 \text{ K}$. The observed changes are attributed to the capture and release of electrons by O-H complexes. Although the H shallow donors can be neutralized at low temperatures to achieve p-type conductivity the incorporation of hydrogen atoms that act as shallow donors should be avoided.

- [1] C. G. Van de Walle, Phys. Rev. Lett. **85**, 1012 (2000).
- [2] D. M. Hofmann, Hofstaetter, A., Leiter, F., Zhou, H., Henecker, F., Meyer, B. K., Orlinskii, S. B., Schmidt, J., Baranov, P. G., Phys. Rev. Lett. **88**, 045504 (2002).
- [3] S. J. Jokela, McCluskey, M. D., Phys. Rev. B **72**, 113201 (2005).
- [4] N. H. Nickel, phys. stat. sol (b) **243**, R51 (2006).

Corresponding author:

N. Nickel
nickel@hmi.de

Electrical detection of coherent ^{31}P spin quantum states in silicon

K. Lips¹, C. Boehme^{1,2}, A.R. Stegner³, H. Huebl³, M. Stutzmann³, M.S. Brandt³

■ 1 HMI, SE1 ■ 2 University of Utah, Physics Department, Salt Lake City, Utah, USA

■ 3 Walter Schottky Institut, Technische Universität München, Garching, Germany

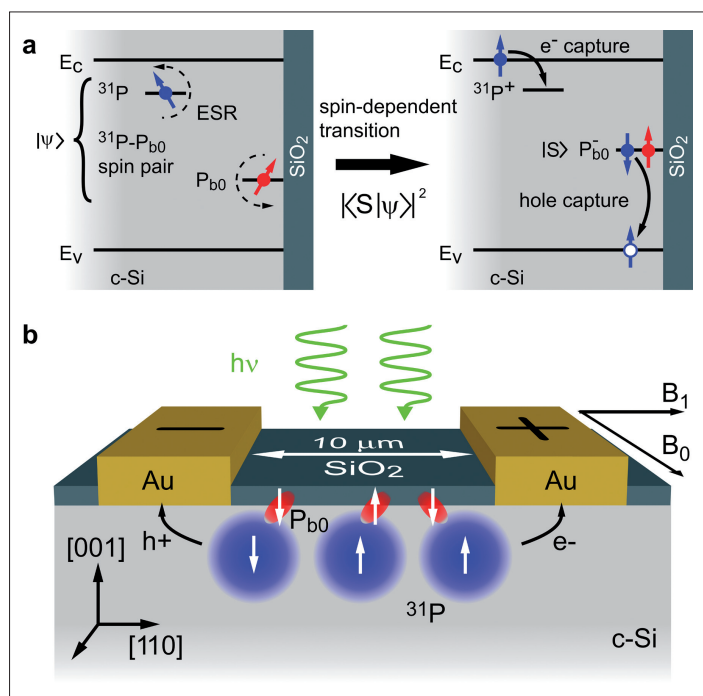


Fig. 1: Read-out scheme for ^{31}P electron spin qubits. (a) Sketch of the band diagram of the Si/SiO₂ interface and the spin-dependent process involving ^{31}P and $\text{P}_{\text{b}0}$ states. (b) Sketch of the Si device used to demonstrate the electrical spin read out [4].

It is the insatiable demand of modern society for energy and information that has strongly promoted two fields of research that seem to be antipodal with respect to the physical requirements involved, namely photovoltaics (PV) and quantum computing (QC), respectively. Whereas in PV a high degree of separation of photo-generated charge is mandatory and not the conservation of coherence¹, the opposite holds for QC. In QCs, information is encoded in quantum states, so called qubits. These qubits are manipulated by a physical procedure that is determined by the

¹ Note that in a PV device charge separation of photo-generated states automatically destroys quantum coherence

mathematical problem that has to be solved. During these manipulations the qubit is not allowed to lose its quantum coherence until the final read-out process. In search of such ideal qubits, the proposal by Bruce Kane [1] of a silicon (Si) based QC where the qubits are formed by the nuclear spin of phosphorus donors (^{31}P) has brought the two research areas closer together due to their common material issues.

One of the key problems of Kane's original concept concerns the actual readout of the ^{31}P quantum state. For this a specific nuclear spin is encoded in the ^{31}P electron spin through hyperfine interaction. Since a single electron spin cannot be detected with common electron spin resonance (ESR) (lack in sensitivity by over 10 orders of magnitude), the realization of spin-to-charge transfer is the key prerequisite for a successful implementation of single spin phosphorus (^{31}P) readout devices, capable of determining the actual spin state (spin up $|\uparrow\rangle$ or spin down $|\downarrow\rangle$). Such a coherent spin-to-charge transfer was experimentally verified for the first time in thin-film silicon absorber layers at HMI using pulsed electrically detected magnetic resonance (pEDMR) [2] and a spin based qubit readout concept was proposed [3] and recently experimentally verified on a 15 nm thin layer of P-doped crystalline silicon (c-Si) (see Fig. 1b) [4]

Fig. 1(a) illustrates the readout scheme based on spin-dependent recombination in silicon. In order to probe ^{31}P electron spins, spin-dependent recombination through $\text{P}_{\text{b}0}$ centers is used. $\text{P}_{\text{b}0}$ centers are trivalent Si atoms at the c-Si/SiO₂ interface that introduce paramagnetic states in the Si band gap. If a neutral $\text{P}_{\text{b}0}$ center is located in the vicinity of a ^{31}P donor, both their electrons can form a coupled spin pair. This spin pair can relax by a transfer of the electron from the ^{31}P to the $\text{P}_{\text{b}0}$, forming a negatively charged defect ($\text{P}_{\text{b}0}^-$). This transition probability depends strongly on the relative spin orientation of the two electrons of the pair. Since the spin configuration can be changed by ESR, the capture probability at the $\text{P}_{\text{b}0}$ can be altered and hence the fingerprint of the paramagnetic states involved can be observed in the photocurrent.

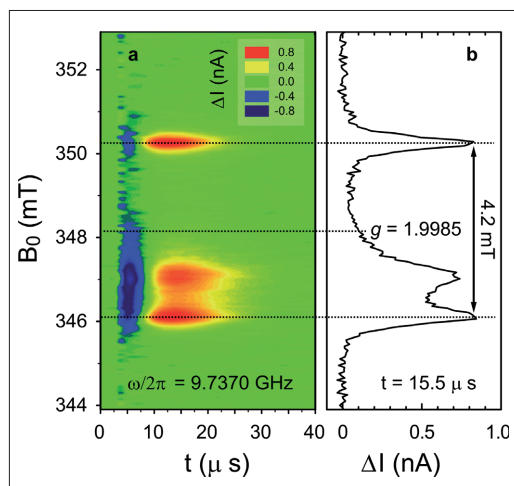


Fig. 2: (a) Contour plot of the photocurrent transient change induced by a short microwave burst at $T=5\text{K}$. (b) Intensity distribution taken at $t = 15.5 \mu\text{s}$ showing the typical ^{31}P ESR fingerprint in the current [4].

Fig. 2a shows the change ΔI of the photocurrent as a function of time t after the ESR microwave pulse was turned off. The plot shows three resonances exhibiting identical dynamics. The intensity plot taken at $t=15.5 \mu\text{s}$ as shown in Fig. 2b clearly shows two hyperfine split features separated by 4.2mT (g value 1.9985). This is the characteristic ESR fingerprint of the ^{31}P donor electron in Si. The two lines stem from the two spin orientations of the ^{31}P nuclear spin. The broader peak at 347.1mT originates from $\text{P}_{\text{b}0}$ centres. When the current behaviour is analysed on the same time scale (ns-scale) as the driving ESR microwave field induces Rabi oscillations between energy levels of the spin pairs, oscillations in the photocurrent are observed (Fig. 3). The fact that the oscillation frequency increases with increasing ESR microwave power indicates that the ^{31}P spin state can be detected coherently in the photocurrent. Rabi echo experiments (not shown) reveal that the fast decay of the Rabi oscillations in Fig. 3 is not due to incoherence but is caused by an inhomogeneous microwave field, which leads to a fast coherent dephasing of the spin ensemble. The true dephasing time was determined to be above $1\mu\text{s}$.

The experiments have been carried out on ensembles of ^{31}P . The charge noise achieved so far is about $10^4 e$ resulting in a detection limit that is around 11 orders of magnitude lower than for conventional nuclear magnetic resonance and about 7 orders of magnitude lower than for ESR. The results shown are an important step towards the

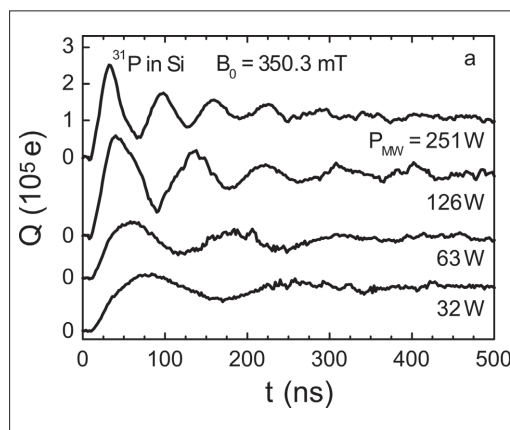


Fig. 3: Rabi oscillation observed at a magnetic field position of 350.3 mT (ESR resonance of ^{31}P) in Fig. 2b for various microwave powers. The Rabi frequency increases linearly with microwave field amplitude. Since the electron spins of ^{31}P and $\text{P}_{\text{b}0}$ are in the triplet state (both spins parallel) before the ESR pulse is applied, the maximum of Q indicates $|\uparrow\rangle$ of ^{31}P , a minimum corresponds to $|\downarrow\rangle$.

realization of an electrical spin readout of donors. The proof-of-principle experiments demonstrate a spin-to-charge transfer mechanism required for ^{31}P electron spin readout via $^{31}\text{P}-\text{P}_{\text{b}0}$ pairs and show that this spin pair is sufficiently weakly coupled so that the ^{31}P hyperfine interaction can be observed, ultimately allowing the electrical detection of the nuclear spin state. However, although inclusion of this readout scheme into a scalable architecture is in principle conceivable via local gates, electrostatically controlling the $^{31}\text{P}-\text{P}_{\text{b}0}$ coupling, there remain a variety of physical and technological issues to be solved before application of the readout scheme to quantum information processing.

- [1] B. E. Kane, Nature **393** (1998) 133
- [2] C. Boehme and K. Lips, Phys. Rev. Lett. **91** (2003) 246603
- [3] C. Boehme and K. Lips, phys. stat. sol. (b) **233** (2002) 427
- [4] A. R. Stegner, C. Boehme, H. Huebl, M. Stutzmann, K. Lips, and M. S. Brandt, Nature Physics **2** (2006) 835

Corresponding author:

K. Lips
lips@hmi.de

Stability of CuInS_2 Module Test Structures under Reverse Bias Stress

Ch. Köble¹, J. Klaer², R. Klenk¹

■ 1 HMI, SE2 ■ 2 HMI, SE3

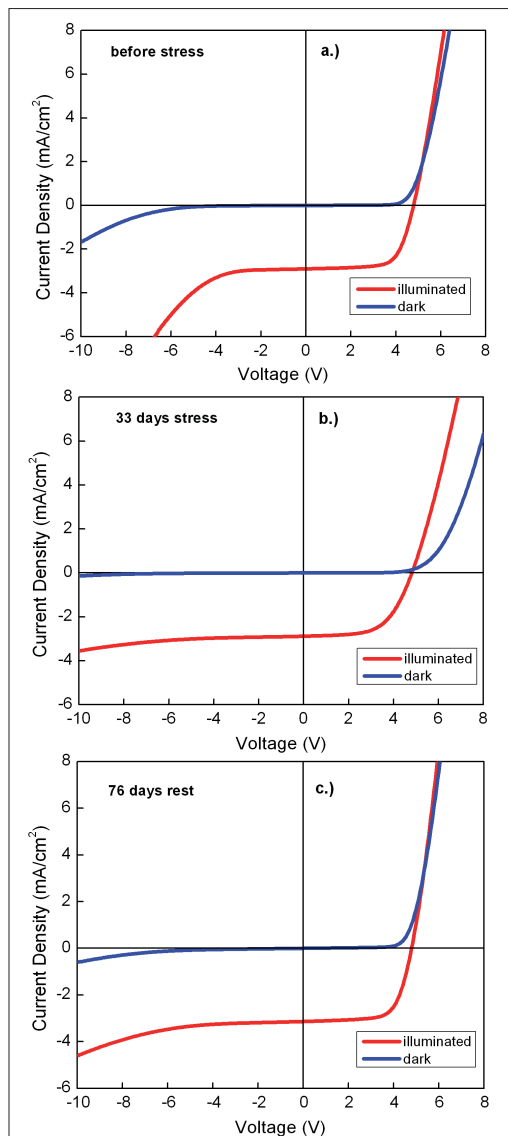


Fig. 1: Voltage-current curves of CuInS_2 module test structures (seven cells connected in series by monolithic integration). After 33 days of reverse-bias stress the rectification properties are enhanced but an apparent series resistance and a distinct cross-over have developed. In the following rest period the forward characteristics are fully restored confirming that there is no permanent damage has been caused.

Thin-film chalcopyrite-based modules are known to maintain a comparably high efficiency when partially shaded. This constitutes a significant advantage over conventional silicon modules and contributes to a high annually averaged output in terms of kWh/kWP even in difficult applications, e.g., building integration. During standard certification procedures (IEC 61646), such as the test

for degradation under ultraviolet light, the module may also be illuminated inhomogeneously. Under any of these conditions, the cells that see little or no illumination are biased in reverse. In this work we have studied the stability of monolithically interconnected test structures (mini-modules) under such conditions. We find that prolonged current flow in reverse direction without illumination modifies the jV -curve of CuInS_2 mini-modules. Rectification properties are significantly enhanced. A degradation of the fill factor is observed immediately after the stress test but the fill factor eventually recovers completely. None of the investigated samples was irreversibly damaged. We conclude that CuInS_2 modules can be operated safely under partial illumination without the need for protection by bypass diodes.

In contrast to Cu(In,Ga)Se_2 -based cells, typical CuInS_2 -based devices show an illumination-dependent reverse breakthrough at relatively low voltages (Fig. 1). In principle this is advantageous because it minimizes the power consumed within a reverse-biased cell. During the stress period, the reverse breakthrough “flattens” as seen in Fig. 1, resulting in a substantial increase of the breakthrough voltage. This could imply that the efficiency CuInS_2 module under prolonged partial shading is not quite as high as previously assumed. The slope of the forward characteristics reduces due to an increasing apparent series resistance, resulting in lower fill factor. In addition we note a more pronounced cross-over between illuminated and dark jV -curves. The open circuit voltage of the mini-modules changed only slightly, and not in a systematic way. The photo current density stayed on the same level. In some cases we observed a spontaneous healing of shunts. After removing the reverse bias from the mini-modules, the samples were stored under un-

specified ambient conditions for recovery. During the recovery period the apparent series resistance diminishes relatively fast. This allows the forward characteristics to recover to the original shape and the fill factor to increase again. In all cases the module performance under illumination was eventually restored or even slightly exceeded the one determined before the experiment. The reverse breakthrough behaved somewhat different. In some cases the reverse characteristics continued the trend observed during the stress period before reversing eventually. In other cases the breakthrough voltage decreased right away, albeit with a very long time constant. Within these experiments we have not seen a single sample where the reverse breakthrough has returned to the original curve, not even after 7 months.

The apparent series resistance in forward direction and more distinct cross-over of dark and light jV -curves are clearly meta-stable effects as the fill factor recovers completely after removing the external bias. In some aspects similar observations have been reported by M. Igalson et al. for Cu(In,Ga)Se₂-based solar cells [1,2]. In their case the jV curve develops a kink or S-shape and the apparent series resistance observed here may be interpreted as a milder case of the same effect. The cross-over between light and dark jV is present in both cases. These non-linear effects were explained by deep acceptors close to the interface and a modification of their occupation probability under non-equilibrium conditions, in extension of a model described earlier by A. Niemegeers et al. [3]. Ionization of the acceptors results in a p⁺ layer impeding the current flow. However, it is assumed for these models that there is a surface layer (ordered vacancy compound, OVC) with a band gap wider than that of the bulk material [4]. Consequently, there is a hole barrier in the valence band which decouples the deep acceptor states in this surface layer from the hole distribution in the chalcopyrite valence band. The non-linear effects in this model depend critically on the existence of such a hole barrier. It is at the moment unclear whether a hole barrier exists in CuInS₂ solar cells. On one hand, the material is prepared under copper excess and more or less lattice-matching OVC phases are not reported

in the equilibrium phase diagram (CuIn₅S₈ has a completely different spinel structure). On the other hand the surface composition after chemical removal of the CuS segregations is reported to be deficient in copper and there are indications of at least a small widening of the surface band gap [5]. A more detailed investigation of the reverse-bias-induced effects could therefore be valuable in clarifying the band structure and recombination mechanisms of CuInS₂ cells in the vicinity of the interface. This is especially valid if a model can be formulated that describes both, modification of the current transport in reverse as well as in forward direction.

-
- [1] M. Igalson, M. Bodegard, L. Stolt, *Solar Energy Materials & Solar Cells* **80** (2003) 195
 - [2] P. Zabierowski, U. Rau, M. Igalson, *Thin Solid Films* **387** (2001) 147
 - [3] A. Niemegeers, M. Burgelman, R. Herberholz, U. Rau, D. Hariskos, H.W. Schock, *Progress in Photovoltaics* **6** (1999) 407
 - [4] D. Schmid, M. Ruckh, F. Grunwald, H.W. Schock, *J. Appl. Phys.* **73** (1993) 2902
 - [5] L. Weinhardt, O. Fuchs, D. Groß, G. Storch, E. Umbach, N.G. Dhere, A.A. Kadam, S.S. Kulkarni, C. Heske, *Appl. Phys. Lett.* **86** (2005) 062109

Corresponding author:

R. Klenk
klenk@hmi.de

Replacing Indium in chalcopyrite-type thin film solar cells by abundant elements

I.M. Kötschau, A. Weber, S. Schorr, H.-W. Schock

■ HMI, SE3

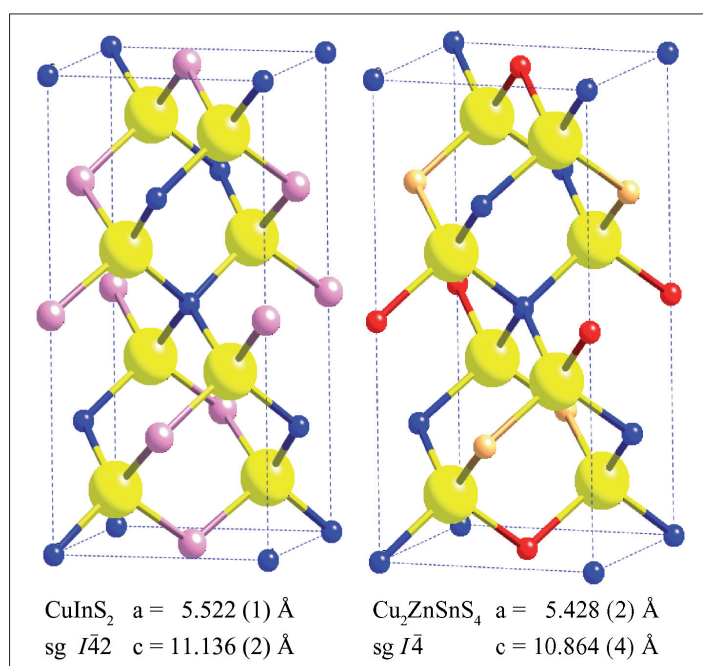


Fig. 1: Comparison of the chalcopyrite type (left) and the kesterite type (right) structure. Both structures show tetragonal symmetry but belong to different space groups (sg). (blue – Cu; pink – In; red – Sn; orange – Zn; yellow – S).

Highly efficient thin film solar cells based on compound semiconducting materials such as $\text{Cu}(\text{In,Ga})\text{Se}_2$ show a current record efficiency of 19.5% on the laboratory scale [1]. Solar cells made of plain CuInS_2 have not reached these record efficiencies yet but are also of significant interest due to a number of advantages in comparison with the more widely investigated selenium containing chalcopyrites. Both, solar cells made of $\text{Cu}(\text{In,Ga})\text{Se}_2$ as well as CuInS_2 , are on the verge to large scale industrial production.

Since the availability of indium is an object of concern regarding the production on a gigawatt scale, its replacement by more abundant elements at similar efficiency is very desirable. An alternative compound for thin film solar cells is kesterite ($\text{Cu}_2\text{ZnSnS}_4$). This compound possesses promising characteristic optical proper-

ties with a band gap energy of about 1.5 eV and a large absorption coefficient in the order of 10^4 cm^{-1} . According to the literature the best conversion efficiency obtained with this compound is 5.45% [2]. The chalcopyrite type structure and the kesterite type structure are closely related but non-isotyp (Fig. 1). The main difference consists in a different cation ordering. Both obey tetragonal symmetry and can be foreseen as substitutional derivative ternaries of the cubic sphalerite type structure.

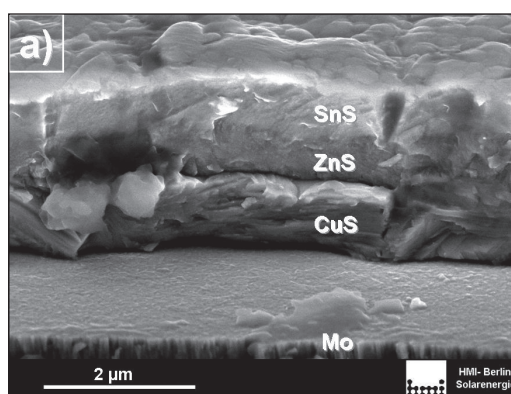


Fig. 2a: Precursor layer of the sequence Mo-CuS-ZnS-SnS (Cu-rich composition). The three layer stack is clearly visible.

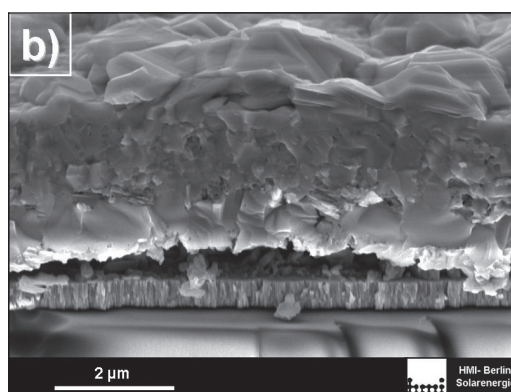


Fig. 2b: Precursor layer after processing according to program in Fig. 3. The copper sulphide (CuS) forms large crystallites on top of the film.

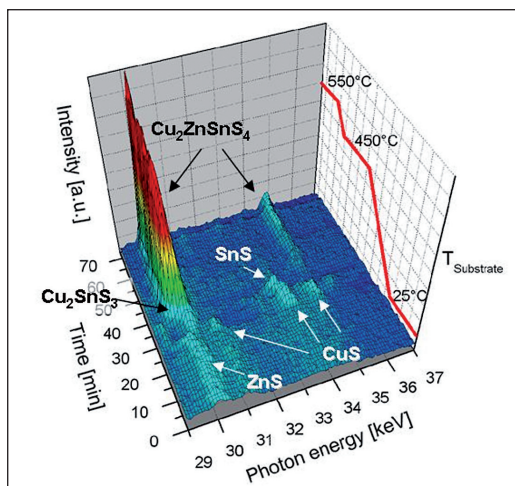


Fig 3: 3D-Plot of EDXRD data gathered during the annealing of the film depicted in Fig. 2b. Before reaching the first annealing period at 450°C most binary sulphides are consumed. At 30 keV the strong diffraction peak of the (densely packed) 112 lattice planes of Cu₂ZnSnS₄ appears. A shoulder of this peak can be assigned to Cu₂SnS₃ and disappears upon further heating to 550°C.

The absorber of the best thin film Cu₂ZnSnS₄ solar cell devices has been processed in two steps. At first a precursor stack with metallic layers or binary sulphides (ZnS, SnS etc.) is deposited by sputtering and evaporation techniques. In the second step the precursor is sulphurized under vacuum conditions at temperatures about 550°C [3]. However, the reactions during the crucial second step of this process have not been investigated yet. Therefore in-situ energy dispersive X-ray diffraction (EDXRD) has been applied to study the formation of Cu₂ZnSnS₄ thin films.

Precursors on Mo-coated glass substrates have been formed by sputtering and sulphurization of copper and subsequently evaporating ZnS and SnS. Different Cu/(Zn+Sn)-ratios and deposition sequences (CuS-ZnS-SnS and CuS-SnS-ZnS) have been investigated. A typical precursor is depicted in Fig. 2a.

The diffraction experiment is based on a process chamber designed for the energy dispersive x-ray beamline F3 at HASYLAB, Hamburg [4]. The setup consists of a pumping system giving base pressures of about 10⁻⁵ mbar in the chamber, a Knudsen cell for sulphur effusion and a sample holder with an integrated ceramic heater. A small polyimide window allows the white synchrotron radiation (meV-100keV at beamline F3) to enter

the process chamber where it interacts with the sample. The scattered light is detected under a fixed angle 2θ of 7.2° by an energy dispersive detector in the range of 5 keV to 57 keV. The substrate temperature rises slowly from room temperature to annealing temperatures of 450°C and 550°C, while sulphur is continuously evaporated from the Knudsen cell to avoid sulphur deficiency in the thin film. Every 15 seconds a complete EDXRD spectrum is recorded which allows one to track the phase sequence in dependence of process time and temperature.

Fig. 3 shows a section of the sequentially recorded EDXRD spectra as a function of energy and time/temperature. The evaluation shows that in a first step (re)crystallisation of binary sulphides occurs. Upon further heating a transition CuS→Cu_{2-x}S and Sn₂S₃→SnS can be detected and the formation of ternary Cu₂SnS₃ and quaternary Cu₂ZnSnS₄ starts. Reaching 550°C the Cu₂SnS₃-share diminishes and the spectra can be assigned to Cu₂ZnSnS₄ and Cu_{2-x}S (Cu-rich composition). Figure 2b shows a cross sectional SEM image of the precursor stack after the sulphurization process. Large crystallites of CuS can be found on the surface, whereas the Cu₂ZnSnS₄-layer underneath appears still rather inhomogeneous with small crystallites. Nevertheless we found little impact of the metal ratio and stacking sequence on the reaction sequence and a strong tendency to form the kesterite structure in all studied cases. This is an encouraging result for the future exploratory investigation of the material as a photovoltaic absorber for thin film solar cell devices. Stepping further the study will be extended to the 2(CuInS₂)-Cu₂ZnSnS₄ system, where the solid solution formation is based on the substitution 2In³⁺ ↔ Zn²⁺ + Sn⁴⁺. The results of these studies will provide a comprehensive knowledge about microscopic and kinetic aspects of the phase transformation and crystal growth in the Cu-(In/Zn,Sn)-S system. In parallel the results will be used to identify cost effective process pathways suitable and for large scale production processes.

- [1] M. Contreras, M. Romero, R. Noufi, *Thin Solid Films*, **551-512**, p.51 (2006)
- [2] H. Katagiri, K. Jimbo, K. Moriya, K. Tsuchida, *Proc. 3rd WCPEC*, p. 2874 (2003)
- [3] H. Katagiri, *Thin Solid Films*, **480-481**, p.426 (2005)
- [4] C. v.Klopmann, J. Djordjevic, R. Scheer, *Journal of Crystal Growth*, **289**, p. 113 (2006)

Corresponding author:

I. Kötschau
koetschau@hmi.de

Improved insight into the microstructure of chalcopyrite-type thin-film solar cells

D. Abou-Ras, M. Nichterwitz, J. Bundesmann, C.A. Kaufmann, S. Schorr, H.W. Schock

■ HMI, SE3

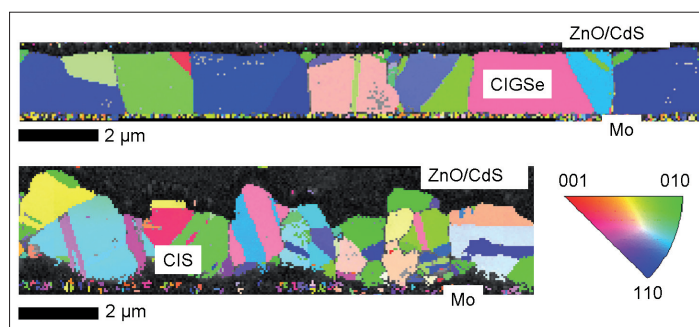


Fig. 1: EBSD maps from ZnO/CdS/CIGSe/Mo/glass (top) and ZnO/CdS/CIS/Mo/glass (bottom) stacks. The colors correspond to various crystallographic directions given by the legend (bottom, right), indicating the local orientations of the CIGSe and CIS thin films. Numerous twins are visible in the CIGSe and CIS layers.

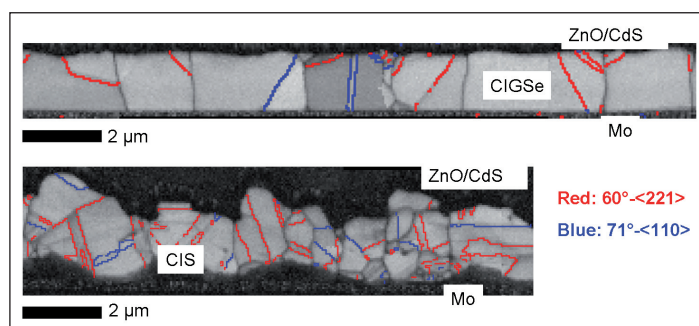


Fig. 2: EBSD maps from ZnO/CdS/CIGSe/Mo/glass (top) and ZnO/CdS/CIS/Mo/glass (bottom) stacks in band contrast (the same sections as shown in Fig. 1). 60° - $\langle 221 \rangle$ twins (red) and 71° - $\langle 110 \rangle$ boundaries (blue) are highlighted.

In research and development of chalcopyrite-type thin-film solar cells, such as, e.g., those based on $\text{Cu}(\text{In,Ga})\text{Se}_2$ (CIGSe) – grown by coevaporation of the elements [1] – and CuInS_2 (CIS) – grown by rapid-thermal annealing [2] –, it is essential to analyze the effect of parameter variations (e.g. deposition temperature or composition) on the microstructure of the absorber and to compare this information with the solar-cell performance. Electron-backscatter diffraction (EBSD) represents a powerful technique to determine grain sizes, grain orientations and grain boundaries in

polycrystalline materials, providing high precision and good statistics. The information gathered on the microstructure in the thin films is of much higher quality than that of, e.g., „apparent“ grain sizes from scanning electron micrographs. Since the current conduction in a thin-film solar cell proceeds perpendicular to the surface, it is important to study the microstructures of chalcopyrite-type thin films in cross-section in order to resolve possible effects of grain sizes and grain boundaries on the electrical properties of the solar cells.

For the first time, EBSD studies have been conducted on polished cross-sections of CIGSe and CIS thin-film solar cells. The EBSD maps shown in Fig. 1 were acquired using a point-to-point distance of 50 nm. The microstructures of the CIGSe and CIS thin films are well resolved. The difference in grain size of both layers is apparent. Numerous twins are visible in both layers, formed probably during growth or during the cool-down phase after the deposition.

The nature of the grain boundaries was determined with high precision. The most frequent types of grain boundaries found in CIGSe and CIS thin films are 60° - $\langle 221 \rangle$ and 71° - $\langle 110 \rangle$ twin boundaries. Both grain-boundary types have a Σ value of 3, which can in general be attributed to lowest grain-boundary energies. In Fig. 2, EBSD maps from ZnO/CdS/CIGSe/Mo/glass (top) and ZnO/CdS/CIS/Mo/glass (bottom) stacks in band contrast are shown with 60° - $\langle 221 \rangle$ (red) and 71° - $\langle 110 \rangle$ twin boundaries (blue) highlighted.

The rotation transformations characterized by 60° - $\langle 221 \rangle$ and 71° - $\langle 110 \rangle$ transform certain $\{112\}$ crystal planes to other $\{112\}$ planes (e.g., (112) to $(\bar{1}12)$); i.e., the most grain boundaries in CIGSe and CIS thin films are coherent or quasi-coherent along $\{112\}$ planes. This fact can be related directly to the importance of $\{112\}$ planes for the topotactical growth of CuInS_2 and $\text{Cu}(\text{In,Ga})\text{Se}_2$ thin films.

Apart from local orientations and grain boundaries, also grain sizes can be determined with high precision. It was found that all grain-size distributions from CIGSe and CIS thin films are rep-

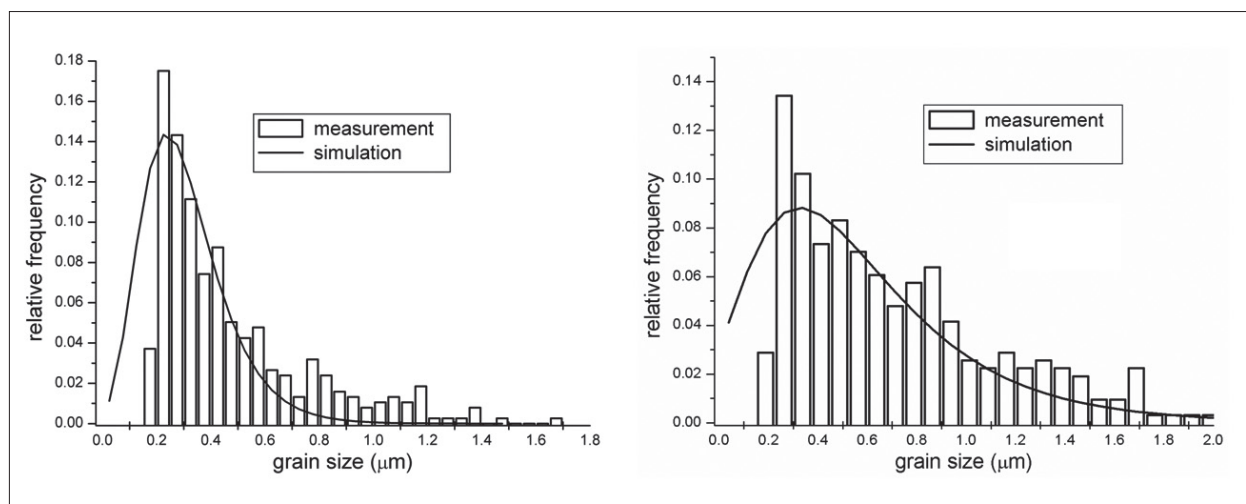


Fig. 3: Grain-size distributions of CIGSe (left) and CIS (right) thin-film absorbers in completed solar cells. The measured grain sizes (bars) can be represented well by lognormal distributions (solid lines).

resented well by lognormal-distribution functions (Fig. 3). According to literature, lognormally distributed grain sizes are typical for surface-controlled growth - the growth mechanism broadly accepted for the CIGSe and CIS thin films studied in the present work.

In conclusion, a detailed study of the microstructure of CIGSe and CIS thin-film solar cells with high precision and good statistics was performed for the first time, acquiring EBSD maps on cross-section samples. The most frequent grain boundaries were identified, and the importance of $\{112\}$ planes during the topotactical growth of the thin films was revealed. Furthermore, grain-size distributions from CIGSe and CIS thin films can be related to the surface-controlled growth of these layers.

The authors would like to thank Peter Schubert-Bischoff (SF1) and Ulli Bloeck (SE4/SF3) for the help with the sample preparation.

- [1] C.A. Kaufmann, T. Unold, D. Abou-Ras, J. Bundesmann, A. Neisser, R. Klenk, R. Scheer, K. Sakurai, H.-W. Schock, *Thin Solid Films*, to be published, doi:10.1016/j.tsf.2006.12.095.
- [2] J. Klaer, R. Klenk, D. Abou-Ras, R. Scheer, H.W. Schock, D. Schmid, W. Eisele, J. Hinze, I. Luck, C.v. Klopmann, A. Meeder, U. Rühle, N. Meyer, *Proceedings of the 21st European Photovoltaic Solar Energy Conference and Exhibition, Dresden, Germany, September 4-8, 2006*, pp.1801-1805.
- [3] D. Abou-Ras, S. Schorr, H.W. Schock, submitted.

InGaAsP/InGaAs double junction solar cells

U. Seidel, B.E. Sağol, K. Schwarzburg, T. Hannappel

■ HMI, SE4

front contact		ARC		n-InGaAs	
window	n+	InP		n-InGaAs	20 nm
top cell		InGaAsP			2 μm
BSF	p	InP			50 nm
tunnel	p++	GaAsSb			15 nm
contact	n++	InGaAs			15 nm
barrier	n+	InP			30 nm
bottom cell		InGaAs			3 μm
BSF	p	InGaAs			25 nm
buffer	p	InP			150 nm
substrat	p	InP			350 μm
back contact					

Fig. 1: Layer structure of the MOVPE-grown low bandgap double junction solar cell. For the serial connection of the bottom cell (InGaAs) and the top cell (InGaAsP) a tunnel diode, made up of n-InGaAs and p-GaAsSb, was used.

Recently, multi-junction III-V solar cells in the form of a triple junction cell grown on a germanium crystal have exceeded the 40% conversion efficiency barrier [1]. Even higher values can be achieved [2], if more than three appropriate sub-cells were realized with optimized band gaps. Theoretical calculations show, that a band gap E_{gap} in the range of 1eV is highly desirable for solar cells with multiple junctions. The idea of an InGaAsP/InGaAs tandem solar cell with low band gaps is to replace the bottom Ge sub-cell of the world record cell by a more efficient double junction bottom cell, and to combine the top and bottom tandem cells by means of mechanical stacking, wafer bonding, or separation of the solar spectrum.

For this purpose, we prepared InGaAsP/InGaAs tandem solar cells monolithically on p-InP(100) in our Aixtron MOVPE reactor (AIX-200), using non-gaseous precursors that are less toxic than the

conventional gaseous precursors. As shown in Fig.1 the serial connection between the InGaAs bottom cell ($E_{\text{gap}} = 0.75\text{eV}$) and the InGaAsP top cell ($E_{\text{gap}} = 1.1\text{eV}$) was realized by an Esaki-diode-like tunneling junction including thin layers of highly n-doped InGaAs and highly p-doped GaAsSb. This asymmetric material combination was used because of their favorable band offsets. For achieving the best performance of the tunnel diode and the solar cell, the interface between the n-InGaAs and p-GaAsSb layers has to be as sharp as possible. Therefore, the influence of different preparation procedures on the InGaAs/GaAsSb-interface was investigated in detail by optical in-situ spectroscopy, i.e. reflectance difference/anisotropy spectroscopy (RDS/RAS). These in-situ signals were benchmarked via a contamination-free transfer from MOCVD to UHV and surface science tools like low energy electron diffraction (LEED) and photoelectron spectroscopy (XPS/UPS).

A sharper InGaAs/GaAsSb-interface was achieved, if the growth of the GaAsSb layer was performed on an InGa-rich surface reconstruction.

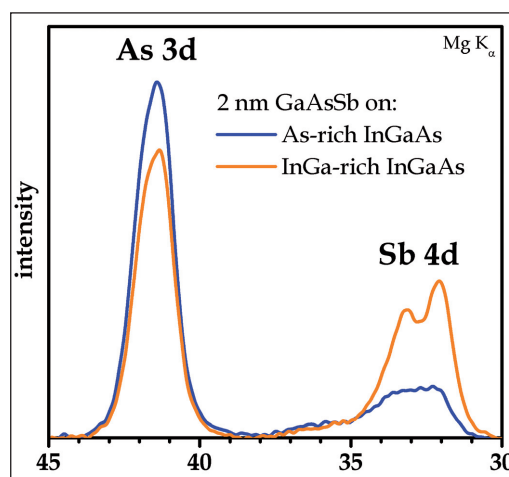


Fig. 2: As 3d and Sb 4d core levels, measured with XPS on 2nm GaAsSb, grown on As-rich (blue) and on InGa-rich (orange) InGaAs surface. The growth on the InGa-rich InGaAs surface leads to more Sb in the GaAsSb layer.

tion. Starting on As-rich InGaAs resulted in a much less Sb content within the first monolayers of the GaAsSb layer, which was detected by XPS (see Fig.2). Analysis of the Sb 4d and the As 3d core level peak areas revealed, that the Sb to As ratio was more than three times higher for the GaAsSb grown on InGa-rich InGaAs, than for the GaAsSb grown on As-rich InGaAs [4]. Direct comparison of these results to a standard As-rich GaAsSb surface [5] showed that the Sb to As ratio of the III-rich interface preparation was much more suitable than the V-rich preparation.

I-V curves of InGaAsP/InGaAs low band gap double junction solar cells are shown in Fig.3. I-V measurements were performed with the in-house solar simulator (SE2). It shows the characteristics under full AM1.5g spectrum (blue curve) and additionally the response to the filtered AM1.5g illumination (red curve). For the filtered measurement a RG850 (Schott) filter was used for simulating the illumination conditions for the operation of the double junction solar cell below a GaAs-based top cell. An open circuit voltage of 840 mV, a short circuit current density of 12.1 mA/cm², a fill factor of 73% and a solar conversion efficiency of 7.3% were obtained without an antireflection coating (ARC).

If this efficiency value is compared with the 4.6% of efficiency, which had been achieved with a germanium sub-cell employed in such a high efficiency triple-junction solar cell (GaInP/GaInAs/Ge) [6], the potential of the InGaAsP/InGaAs double junction solar cells is obvious. By the optimization of the absorber layer thickness and the AR-coating, an improvement of the efficiency for filtered sunlight to around 10% should be possible. In combination with a GaAs-based high bandgap multi-junction solar cell, a total conversion efficiency around 45% could be achievable.

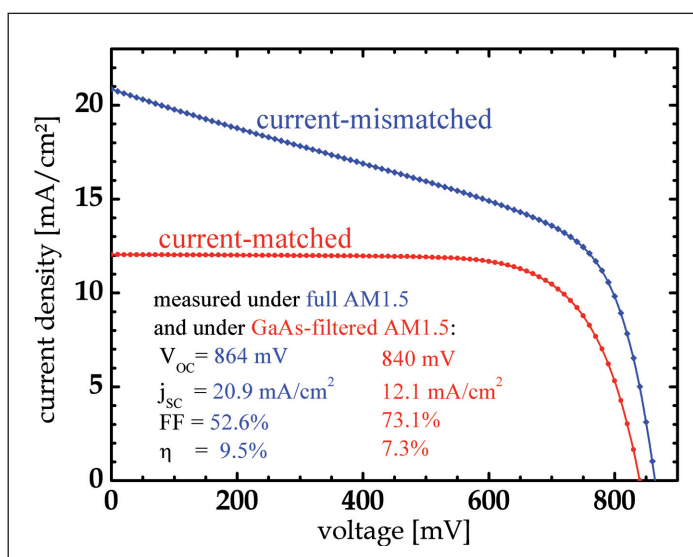


Fig. 3: I-V characteristic of an InGaAs/InGaAsP double junction solar cell measured under a full (blue curve) and a RG850-filtered (red curve) / spectrum.

- [1] <http://compoundsemiconductor.net/articles/news/10/12/5/1>
- [2] A. Marti, G.L. Araujo, Solar Energy Materials and Solar Cells **43** (1996) 203
- [3] F. Dimroth, C. Baur, A.W. Bett, K. Volz, W. Stolz, Journal of Crystal Growth **272** (2004) 726
- [4] U. Seidel, H.-J. Schimper, Z. Kollonitsch, K. Möller, K. Schwarzburg, T. Hannappel, J. Cryst. Growth **298** (2007) 777-781
- [5] Z. Kollonitsch, H.-J. Schimper, U. Seidel, K. Möller, S. Neumann, F.-J. Tegude, F. Willig, T. Hannappel, J. Crystal Growth **287** (2006) 536-540
- [6] C. Baur, M. Meusel, F. Dimroth, A. W. Bett, Conference Record of the 31st IEEE PV Specialists Conf., IEEE, Piscataway, NJ, USA 2005 675

Electrical Response of Wet Chemically Grown ZnO Nanorods for Photovoltaic Applications

J. Tornow¹, K. Ellmer², K. Schwarzburg¹

■ 1 HMI SE4 ■ 2 HMI SE5

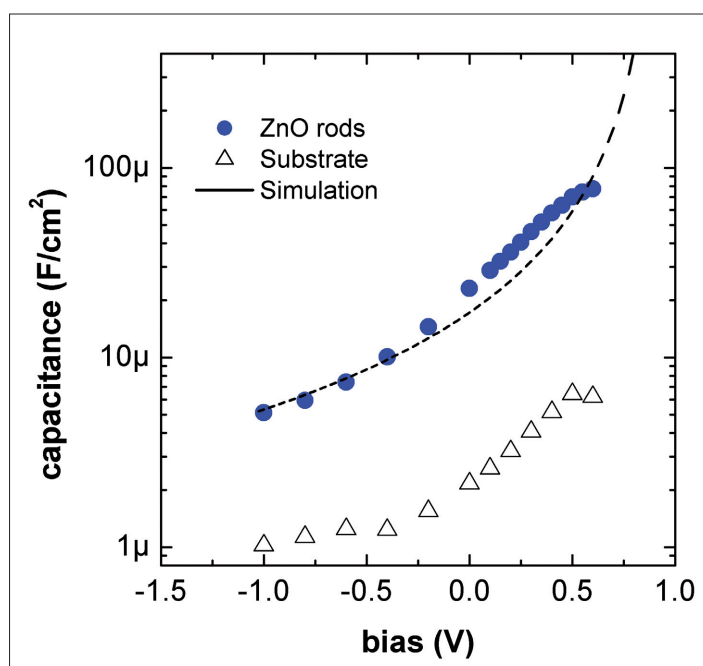


Fig. 1: Bias dependent capacitance of a nanorod electrode (filled circles) and the substrate alone (open triangles).

Vertically aligned ZnO nanorods were reported recently as an alternative oxide substrate for a dye sensitized solar cell (DSSC) [1] and for solar cells with extremely thin solid state absorbers [2]. Replacing the network of TiO₂ nano colloids in standard DSSC is expected to bring improvements in charge carrier transport due to the much higher electron diffusion coefficient of ZnO. The open rod structure gives a much greater flexibility in deposition processes for the application in a ultra thin absorber solar cells. ZnO nanorod electrodes can be grown by several methods ranging from gas phase epitaxy on patterned substrates that gives nearly perfectly aligned periodic structures to low cost methods like chemical bath deposition. We have prepared Zinc oxide nanorod electrodes by covering a fluorine doped tin oxide glass substrate with a compact layer of sputtered

ZnO and subsequently placing this substrate in an aqueous solution containing Zn(NO₃)₂ (0.01M) and NaOH (0.36M) at 80°C. Using different growth times of 5 to 120 minutes resulted in rod lengths of less than 0.5 μm up to more than 2 μm with typical rod diameters ranging from 10 nm to 200 nm. Samples were post annealed at 450°C for one hour. First experiments indicate that these electrodes are indeed a very promising candidate for ultra thin absorber solar cells with respect to inner geometry (aspect ratio~10-20), scalability and potential costs. Knowledge about electronic properties of the ZnO nanorod material and electrical behavior in test devices is essential for the successful development of such solar cells. We have carried out extensive electrical measurements and simulations to better understand in particular the role of the geometry on the electrical response. An easy method to measure the electrical response of the ZnO nanorod electrodes is to employ them in a dye sensitized solar cell configuration [1]. By measuring stationary currents, impedance and photocurrent transients of such DSSC test devices it turned out, that the ZnO nanorod electrode contributes a capacitive component to the electrical response of the cell. Compared to most other solar cells the full frequency (0-10MHz) and time response (t>5ns) is rather complicated but can be modeled very well by making reasonable assumptions. The cause for the complicated response is the large capacitance of around 10 μFcm⁻² for a ZnO electrode with an aspect ratio of ~10. The low impedance of the ZnO electrode makes the cell response sensitive to other low impedance elements in the cell, in particular the counter electrode in the DSSC configuration. Nevertheless, by studying the bias dependency of the impedance response or the photocurrent response under varying amounts of additional series resistors, the ZnO capacitance could be identified.

Fig.1 shows the bias dependency of the ZnO capacitance extracted from an impedance measurement. The measured capacitance scales linearly with the length of the nanorods (not shown

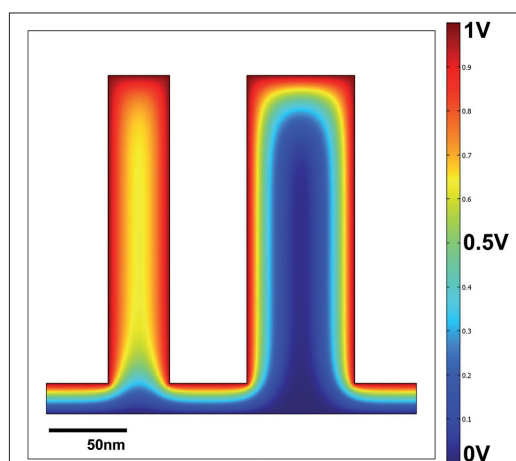


Fig. 2: Simulated potential distribution in a thin (40 nm) and a thick (80 nm) nanorod at 1V voltage drop across the interface for a charge carrier concentration of 10^{18}cm^{-3} .

here). While the overall transient response of the cells is almost as slow as in genuine Grätzel cells using the nanoporous TiO_2 substrate, it is not related to a slow electron transport in the ZnO but rather to the stationary electron distribution in the ZnO . The latter is evident by considering that the ZnO rods could be modeled with a static capacitance and by considering the bias- and rod-length dependencies of the capacitance values. It is instructive to visualize the distribution of the electrical potential in a nanorod. Fig.2 shows a FEM simulation of the potential distribution for thin and thicker rods with an electron concentration of 10^{18}cm^{-3} at 1V potential drop between the substrate and the rod. The potential drop inside the 40 nm thin rod is small and corresponds to a very low electron concentration. This almost field free situation is the accepted scenario for the colloid based DSSC solar cell. Since the assumed intrinsic electron concentration is rather high, an increase in the rod diameter to 80 nm already establishes a depletion layer inside the rod. The electron concentration in the middle of the rod

is close to the intrinsic value (10^{18}cm^{-3}). Clearly, from the measurements (Fig.1) we can conclude that this is also the case for at least the majority of thicker rods in our electrodes. By calculating the carrier distribution at various potentials one can construct a plot of the rod capacitance vs. the voltage bias. A carrier density of around 10^{19}cm^{-3} and an average rod diameter of 80 nm gave a rough fit to the data (Fig.1 'simulation'). Depending on the actual values, the typical rod diameters of 10 – 100nm and carrier densities of 10^{17}cm^{-3} – 10^{19}cm^{-3} for ZnO rods can easily produce either the 'fully depleted' or the 'depletion layer' case. It is not yet clear which one of the 2 cases is favorable for a nanorod solar cell. This will depend on several factors such as the magnitude of tunneling currents and needs to be studied further both theoretically and experimentally.

- [1] M. Law, L. Greene, J. Johnson, R. Saykally, P. Yang, *Nature Materials* **4** (2005) 455-459.
- [2] C. Levy-Clement, R. Tena-Zaera, M. Ryan, A. Katty, G. Hodes, *Advanced Materials* **17** (2005) 1512-1515.

Corresponding author:

K. Schwarzburg
schwarzburg@hmi.de

Preparation and analysis of III-V on Si(100) growth

T. Bork, T. Hannappel

■ HMI, SE4

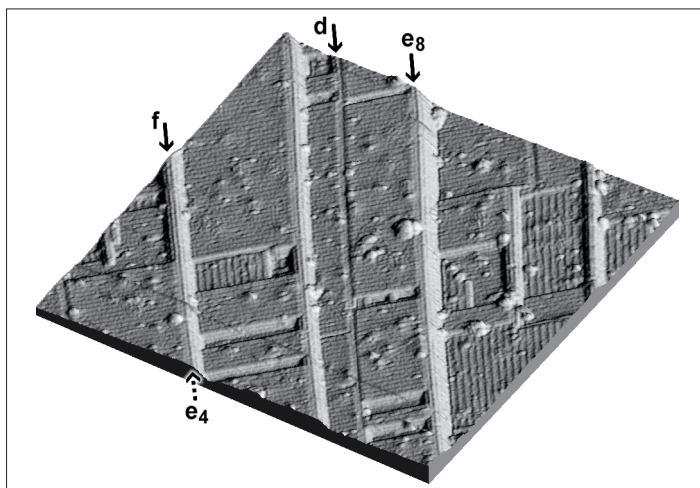


Fig 1: This surface was annealed at 725°C under 42 mtorr AsH_3 . ‘5-7-5’ line structures partially relieve tensile stress generated by As-As dimers. Four representative structures have been labeled (corresponding to Figure 2). Shallow craters form where AsH_3 -etching of a terrace converts a step into a ridge (‘e4’ into ‘f’, for example). The subscripts ‘4’ and ‘8’ indicate step height in monolayers (1 ML = 1.36 Å).

For various applications of III/V-based devices and for the integration with the mature silicon (Si)-technology, the successful hetero-epitaxial growth of III-V films on Si(100) substrates are a prerequisite. High-efficiency multijunction solar cells on Si for example have long been a goal of researchers in the field of photovoltaics. Here, different stages of the III-V nucleation occurring during the metamorphic growth of InP on Si(100) surfaces were studied. The arsenic terminated Si(100) (As:Si(100)) surface is the standard starting point of most state-of-the-art III/V on Si growth procedures, even for III/V compounds that do not contain As. Hence, the As:Si(100) surface has been investigated as a possible substrate for the integration of III-V devices with Si-based technologies. As:Si(100) surface structures were observed with surface sensitive tools like scanning tunneling microscopy (STM), low-energy electron diffraction (LEED), reflectance difference/anisotropy spectroscopy (RDS/RAS), and photoemission (PES) after preparation of the

As:Si(100) surface with metal organic chemical-vapour-deposition (MOCVD). The thus emerging As:Si(100) surface structure is completely different compared to the surface structure developing via preparation in ultra-high-vacuum (UHV) with molecular beam epitaxy (MBE) [1].

Various preparation procedures of the initial III-V on Si(100) nucleation were applied, in-situ monitored via RDS, and benchmarked in UHV employing a contamination-free MOCVD to UHV transfer system [2]. For the first time, tertiarybutylarsine was employed as non-gaseous, much less-toxic precursor compared to arsine to prepare clean arsenic-terminated Si(100). Cleaning of the surface and deoxidation occurred at temperatures of around 900°C, which is significantly lower than it is known for UHV (MBE) preparation [3]. The thickness of the passivating As-termination was about one atomic monolayer. Even and odd-numbered atomic steps occurred on the surface always resulting in a (2x1)/(1x2) two-domain surface (Fig.1). The domain structure of the Si(100) surface was independent from the angle and the degree of the misorientation, also including exactly oriented Si(100).

Different, non-bulk-like double row structures were observed on the As-terminated Si(100) surface via STM. These double row structures have been modeled and described theoretically as so-called ‘5-7-5’ atomic ring structures at the National Renewable Energy Lab by McMahon et al. [4], where concomitant studies have been performed in collaboration in perfect agreement. In these studies, an entire family of trenches, ridges and steps on the nanometre-scale has been observed on TBAs- and AsH_3 -exposed Si(100) (Fig. 2). These atomic ring structures do not appear on Si(100) surfaces treated with pure arsenic. They are energetically favorable compared to MBE-prepared bulk-like steps and flat surfaces and occur at steps, trenches, and ridges. These lines are very long and straight, and could potentially serve as templates for nanowires. Theoretical modelling showed that they are all built around a stress-relieving ‘5-7-5’-ringed atomic structure in which two 5-atom rings bracket a central 7-atom ring (Fig.2). ‘5-7-5’ line structures

partially relieve tensile surface stress generated by As-As dimers. MOCVD-sample preparation was particularly favourable for the formation of '5-7-5' structures. The most reasonable explanation is that AsH_3 decomposition at the surface releases atomic H, which converts Si into SiH_4 . Atomic H released by AsH_3 decomposition also explains why the Si deoxidisation temperature can be lowered significantly below 900°C in an TBAs or AsH_3 flux [3]. No modelling was ever done, because no model existing at the time fit with experimental observations. Here, the energetic stability of '5-7-5' structures, structures ,a', ,b', ,d', and ,e' of Fig. 2, were modelled theoretically using the Plane-Wave Pseudopotential Method with projector-augmented waves [4].

In-situ reflectance difference (RD) spectroscopy signals taken of the As-terminated Si(100) surface showed the same fingerprint as single-domain, (2×1) -reconstructed surfaces obtained in UHV via MBE by Kipp et al.[5], although LEED images of samples prepared in this work displayed a $(2\times 1)/(1\times 2)$ two-domain surface. For the first time, temperature-resolved RD spectra down to 20 K were measured and did not show any energetic shift of the RDS peaks [6]. Thus, the origin of the RD spectra appears to be different from the attribution made by Kipp et al. in their theoretical calculations, i. e. electron phonon interaction and reduced lattice vibration [6].

On the two-domain, As-terminated Si(100) surface a 40 nm InP nucleation layer and, finally, a $>1\ \mu\text{m}$ P-rich state-of-the-art InP film was grown that displayed a (2×1) , single-domain structure [6]. AFM displayed that the nucleation layer was formed by about 20-400 nm crystallites with orientations parallel to the crystal axis. The defect density of the InP film was dependent on the size of these crystallites. For the first time, the entire growth process was monitored with in-situ RDS [6].

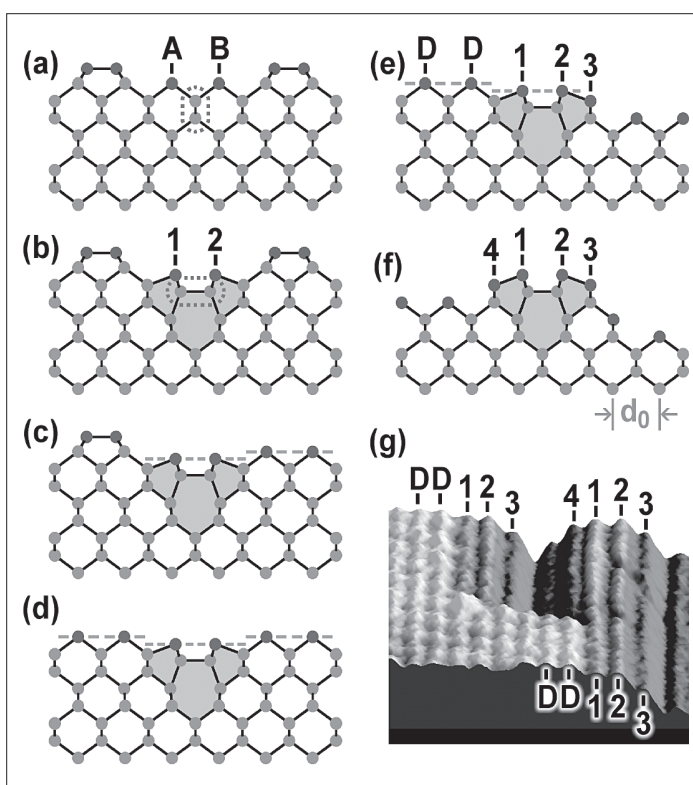


Fig. 2: Structures ,a' -,f': (a) Bulk-like type-A trench, (b) '5-7-5' type-A trench, (c) '5-7-5' 1-ML type-A step, (d) '5-7-5' type-B trench, (e) '5-7-5' type-B step, and (f) '5-7-5' ridge. As-As dimer bonds on the left-side terrace are either perpendicular (type 'A') or parallel (type 'B') to the line structure. All surface atoms are triply-bonded As (dark gray). All sub-surface atoms are quadruply-bonded Si (light gray). (g) STM image, artificially illuminated from the right. Continuity of a '5-7-5' core structure is seen where AsH_3 -etching of the upper terrace has converted part of a type-B step into a ridge. To better show height differences, the ratio of height to width has been increased by 72%. $V_{\text{sample}} = -2.5\ \text{V}$, $I_{\text{tun}} = 0.04\ \text{nA}$.

- [1] T. Bork, W.E. McMahon, J.M. Olson, T. Hannappel, *J. Cryst. Growth* **298** (2007) 54
- [2] T. Hannappel, S. Visbeck, L. Töben, F. Willig, *Rev. Sci. Instrum.* **75** (2004) 1297.
- [3] T. Hannappel, W.E. McMahon, J.M. Olson, *J. Cryst. Growth* **272** (2004) 24
- [4] W.E. McMahon, Iskander G. Batyrev, T. Hannappel, J.M. Olson, S.B. Zhang, *Phys. Rev. B* **74** (2006) 033304
- [5] L. Kipp, D.K. Biegelsen, J.E. Northrup, L.-E. Swartz, R.D. Bringans, *Phys. Rev. Lett.* **76** (1996) 2810.
- [6] T. Bork, PhD theses (2006) HU Berlin

Corresponding author:

T. Hannappel
hannappel@hmi.de

Fractal Photocorrosion of Silicon

M. Lublow and H.J. Lewerenz

■ HMI SE5

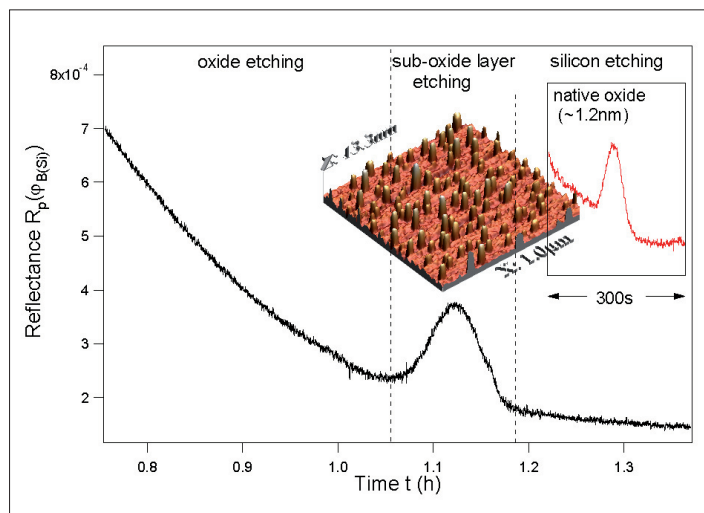


Fig. 1: Time dependence of the in-situ reflectance of thermally oxidized Si(111) at the bulk Brewster angle for $\lambda=500\text{nm}$ (photon energy 2.48eV) in $40\% \text{NH}_4\text{F}$ at open circuit potential. Inset: corresponding curve for native silicon oxide and AFM image of reaction products sticking to the surface during fast sublayer etching.

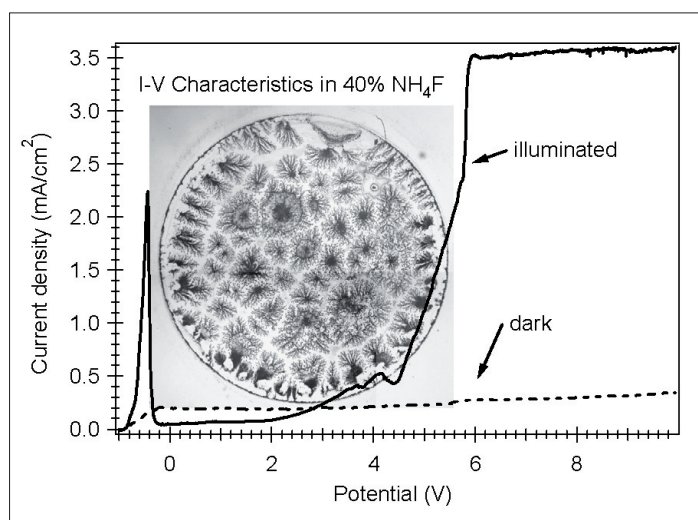


Fig. 2: Photocurrent-voltage curve for n-Si(111) in $40\% \text{NH}_4\text{F}$, $\text{pH}\sim 8$; light intensity 5mWcm^{-2} ; scan rate 10mVs^{-1} ; potential vs. Ag/AgCl electrode. Inset: micrograph of the sample (diameter 0.8cm) after electrochemical treatment.

Fractal patterns are wide spread in nature and occur when a perpetual (or abrupt) driving force interferes with obstacles that hinder unlimited forward-moving. Splitting and fractioning of the motion is then a strategy to overcome the boundaries while the process as a whole starts to exhibit recurring geometrical shapes [1]. Self-similarity and periodicity of these patterns turn out to be a possible consequence and are more than of pure mathematical interest. Diffusion phenomena along liquid interfaces, crystalline- or plant growth, dielectric breakdown effects, the ramifying structures of blood or pulmonary vessels, or even fluctuations in economical systems are examples for and accessible to the methods of fractal mathematics. As for silicon, many processes have already been discussed in terms of fractal analysis: surface roughening phenomena, the formation of porous silicon, or pattern recurrence during (electro-) deposition [2-4]. Recently, unusual anisotropic etching effects were observed while studying the morphological change of the silicon oxide/silicon interface during anodic polarization in concentrated ammonium fluoride. Depending on the process parameters, either etch grooves, following the formation mechanism of Diffusion Limited Aggregation (DLA) theory [5], or microfacet ensembles of high symmetry were produced (see below). As a possible application, fractal microfacet formation suggests an alternative route for (photo-) lithography techniques in the field of Microelectromechanical Systems (MEMS) and High Aspect Ratio (HAR) micromachining due to its inherent self-organization principle.

It is well known that crystalline silicon can be prepared atomically smooth using concentrated ammoniumfluoride solutions [6]. The treatment leaves a surface that exhibits single step atomic terraces and, on (111) surfaces, an $\text{H}(1\times 1)$ lattice termination. Recently, we found in Brewster angle analysis of the etching behaviour of thin and ultrathin silicon oxides that a transitory regime with an enhanced etch rate exists [7]. This effect can be related to the roughening and fast dissolution of a strained layer underneath the silicon/silicon oxide interface that contains further suboxides [8]. For etching of a thermal oxide (18.2nm thickness), for instance, the dissolution of this sublayer commences after 60 minutes exposure and its duration can reach 6 minutes (see Fig.1).

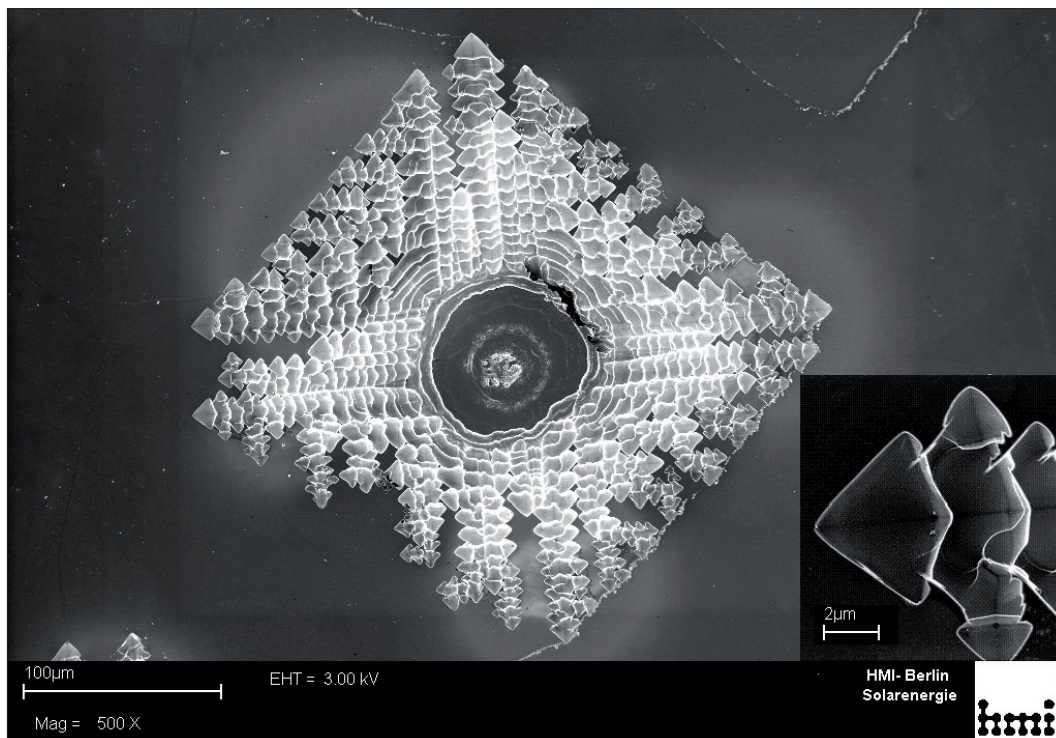


Fig. 3: HR-SEM image of a Si(100) surface after 10 min in 40% NH_4F at 6V; light intensity 7.5mWcm^{-2} . Inset: magnification of (111)-microfacets.

Whereas the surface topography associated with the OCP (open circuit potential) etching shows statistical roughening, a drastically different behaviour was found when the n-silicon electrode is anodically polarized and illuminated: in the plateau range shown in Fig.2, reaching from 5.5V-10V, novel unexpected structures are found that are obviously correlated to the underlying crystal geometry. Figs.3 and 4 show HRSEM images of photocorroded (100) and (111) surfaces after 10 min treatment in the electrolyte. From a circular and nearly unetched area in the center, ramifying etch grooves were initially formed. Enhanced three-dimensional anisotropic etching exposed low-index planes which are assumed to point towards $\langle 111 \rangle$ - direction for the Si(100) sample. A more complex ensemble of facets was found on Si(111) samples (Fig. 4). The overall structure reflects the Bravais-geometry of the respective crystal surfaces, i.e. the square and hexagonal lattice structure, respectively. In Fig.5, a profilometric image of a corroded (100) surface is displayed. The grooves have an almost uniform depth of $\sim 6\mu\text{m}$. Three-dimensional etching has not yet finished to expose the (111)-facets.

Preliminary element analysis by EDX shows silicon oxide and fluoride signals on the surface indicating that the dissolution process is not divalent,

i.e. occurs via direct dissolution of silicon without an oxide intermediate. The process appears to have some similarity with electropolishing where an ultrathin oxide resides on the surface during silicon dissolution. The oxide thickness for the

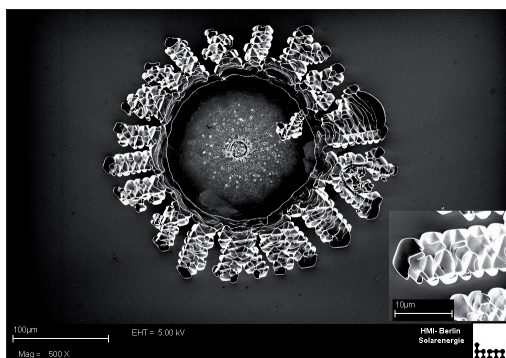


Fig. 4: HR-SEM image of a Si(111) surface after 10min in 40% NH_4F at 6V; light intensity 7.5mWcm^{-2} . Inset: ensemble of periodic microfacets, inclined by different angles with respect to the mean surface plane.

fractal structures is about 5 times larger and, in contrast to electropolishing, the sample roughens in a distinct manner. A marked difference is the observation of oxygen evolution where in the

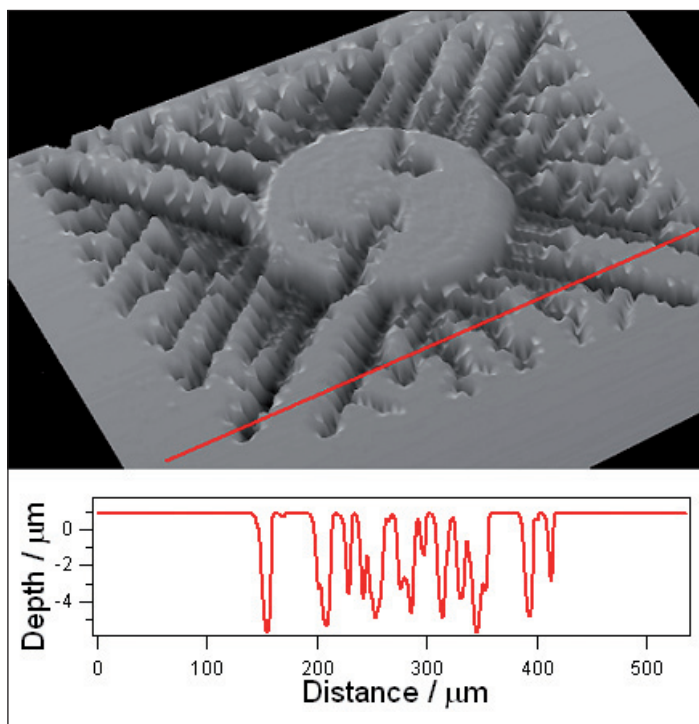


Fig. 5: Profilometric image of Si (100) after 10min in 40% NH_4F at 6V; light intensity 5mWcm^{-2} . Etch grooves have 4-6 μm depth. Three-dimensional etching has not yet exposed the microfacets (compare Fig. 3).

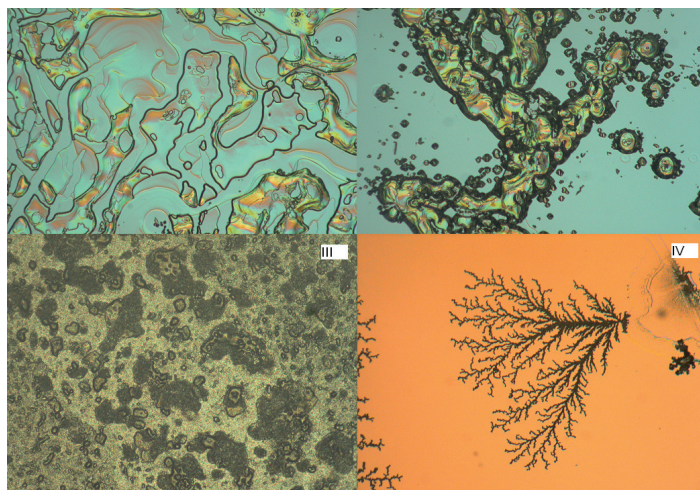


Fig. 6: Assorted micrographs ($\sim 1\text{mm} \times 1.3\text{mm}$) of different surface topographies after anodic (photo-)corrosion in 40% H_4F at 6V: I) p-Si(111); II) p-Si(110); III) n+-Si(111), all experiments in the dark; n-Si(111), illuminated, light intensity 5mWcm^{-2} .

center and at the periphery of O_2 bubbles residing on the surface (see Figs.3, 4) photocorrosion is initiated. Successive corrosion is highly anisotropic with a lateral dissolution rate that exceeds that for perpendicular processes by a factor of ~ 30 . Also, all observed structures, independent of their sizes, can be attributed to smooth atomic facets. In a separate experiment on p-Si, we show (Fig.6, I, II) that distinctively different topographies are obtained for high supply of holes (in this case majority carriers). This points to a charge transport limited process for the creation of fractal structures with illuminated n-Si. Presently, models which incorporate minority carrier trajectories, oxide formation and porosity and diffusion limited etching/aggregation are derived to describe the morphology. Optical properties of these structures, also w.r.t. light harvesting, will be investigated.

- [1] Mandelbrot B. B., 'The Fractal Geometry of Nature', Freeman, New York, 1982
- [2] L. Spanos, Q. Liu, E. A. Irene, T. Zettler, B. Hornung, J. J. Wortman, J. Vac. Sci. Technol. **A12** (1994) 2653
- [3] V. M. Aroutiounian, M. Zh.Ghoolinian, H. Tributsch, Appl. Surf. Sci., **162-163** (2000) 122-132
- [4] M. Zhang, G. Zuo, Z. Zong, H. Chen, Z. He, C. Yang, D. Li, G. Zou, Appl. Phys. Lett. **88** (2006) 203106
- [5] Witten, T., and Sandler, L., Physical Review Letters **47** (1981) 1400
- [6] G. S. Higashi, R. S. Becker, Y. J. Chabal, and A. J. Becker, Appl. Phys. Lett., **58** (1991) 1656
- [7] M. Lublow, H.J. Lewerenz, Surf. Sci. (2007), doi: 10.1016/j.susc.2007.01.038 (in press)
- [8] A. Roy Chowdhuri, Dong-Un Jin, J. Rosado, C. G. Takoudis, Phys. Rev. **B 67** (2003) 245305

Corresponding author:

H.J. Lewerenz
lewerenz@hmi.de

Surface modified ruthenium nanoparticles: a promising cathode catalyst for fuel cell application

G. Zehl¹, I. Dorbandt¹, H. Tributsch¹, P. Bogdanoff¹, S. Fiechter¹, A. Hoell², S. Haas², B. Tesche³

■ 1 HMI, SE5 ■ 2 HMI, SF3 ■ 3 Max-Planck-Institut für Kohleforschung, Mülheim a. d. Ruhr

Fuel cell and catalysts

In the development of devices for an efficient and environmentally compatible conversion of chemical energy into electrical power polymer electrolyte membrane fuel cells (PEM-FC) play a leading part. A wider utilisation of fuel cell modules for mobile power supply systems as well as for stationary applications is of high economic interest, as documented by world wide research activities. However, a commercially wide spread application of PEM-FCs is still impeded by high costs due to the utilisation of expensive membranes (e.g. NAFION®) and of noble metal based catalysts such as platinum. Therefore, cost reductions from increased fuel cell efficiencies as well as an improved system design are major topics of recent research activities.

Besides the phenomenon of instabilities of platinum based catalysts in PEM-FCs leading to a significant power drop at operation time above 1000 hours it is also warned against possible limitations in platinum supply in the long-term. Presuming 1.5 g platinum being needed for 1kW power, a gap of about one order of magnitude is assumed between the availability of platinum in reconnoitred ore deposits on the one hand and the worldwide platinum demand on the other. The distinct disparity between the high quantities of platinum needed and its limited availability reveals the relevance to develop alternative catalysts for PEM-FCs with reduced platinum content or, even more desirable, without any utilisation of platinum at all.

As recently successfully demonstrated, ruthenium based catalysts modified with selenium also exhibit high catalytic activity for the oxygen reduction reaction in fuel cells [1]. One advantage of ruthenium is that it is by a factor of 40 more common in the earth crust and its price presently amounts to only 17% of that of platinum. Furthermore, in Direct Methanol Fuel Cells (DMFC) the undesired crossover of methanol through

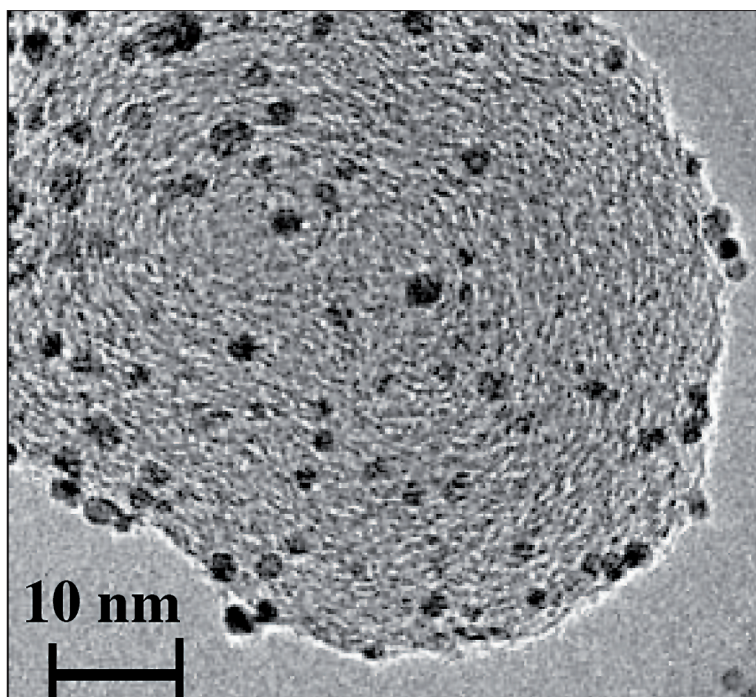


Fig. 1: Transmission Electron Micrograph of platinum particles on the surface of a soot support [1].

the membrane from the anode space into the cathode compartment is still an unsolved issue. Therefore, platinum cathode catalysts suffer from activity losses due to methanol oxidation. As alternative, carbon supported ruthenium nanoparticles modified with selenium feature absolute methanol tolerance. Although intense studies of these catalysts were performed during the last decade, no definite conclusion with respect to the nature of the catalytically active sites and the constitution of the RuSe nano-particles could be drawn. But only a better understanding of the underlying principles is believed to pave the way towards higher active catalysts, thus making DMFCs more efficient and reliable.

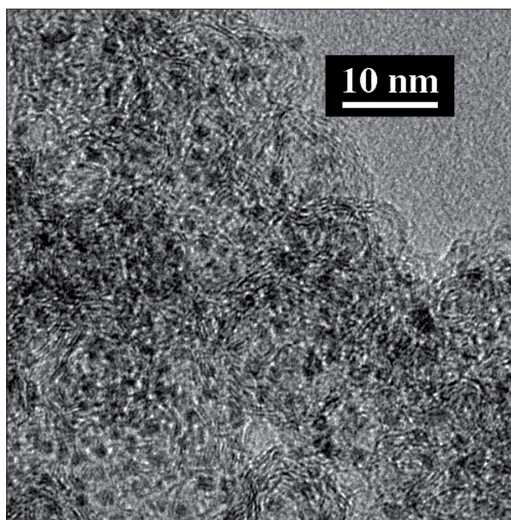


Fig. 2: Transmission Electron Micrograph of selenium modified ruthenium particles embedded in a thermally pre-activated carbon Black Pearls 2000® substrate.

Particle size and carbon support in electro-catalysts

Electrocatalysts in a fuel cell typically consists of two components:

- a carbon support (soot) allowing electrons to migrate from or to the catalytic centers passing an electric consumer and
- nanometer sized particles of a transition metal or cores of metal complexes attached to or integrated in the carbon support to guarantee efficient electron transfer.

Under fuel cell conditions, platinum nano-particles migrate on the surface of the carbon support. Therefore, it is observed that nano-sized particles coalesce after a short time forming larger particles. Since the catalytic activity is corroborated with the number of active sites on the metallic nano particle surface, the catalytic activity of such a catalyst decreases with decreasing surface. It has been demonstrated that ruthenium nano-particles can be properly fixed into nano-groves of the carbon support so that no migration of the metallic particles can occur. Fig. 1 shows a soot particle with an onion like structure of the carbon lattice planes with platinum particles on top of its surface [2]. In Fig. 2 the situation is illustrated for ruthenium particles embedded in the highly structured carbon matrix obtained via CO₂-activation.

While the Pt particles in Fig. 1 are located on the smooth outer surface of the carbon support

RuSe_x counterparts are found within easy accessible nano-cavity of a random oriented graphene layer network.

Structural analysis by X-ray scattering methods

Investigating RuSe electrocatalysts, data about the Se distribution over the catalyst's surface are particularly aspired, because catalytic activity and long term stability strongly depend on the Se content of the RuSe catalysts and the interaction between these two metals. Anomalous Small Angle X-ray Scattering (ASAXS) represents a powerful tool that yields structural parameters for element sensitive analysis of nano-structures, whereas also useful data about the chemical composition in the sub-nanometer scale can be obtained. Using the ASAXS technique one takes advantage of the so-called anomalous or resonant behaviour of the atomic scattering amplitude of an element near its absorption edge to separate its scattering contribution from other elements containing in the sample.

To clarify the structural features of the catalytically active Se-modified ruthenium nano-particles, carbon supported RuSe catalysts were prepared by impregnating a previously CO₂ activated commercial carbon black (Black Pearls 2000® from Cabot) with RuCl₃ followed by reduction under hydrogen. Se modification of this Ru/C intermediate (ruthenium particle size 2-4 nm) was done by impregnation with SeCl₄ and subsequent reductive annealing at 800°C.

A complete set of samples, including the final working RuSe catalyst, and some intermediate preparation states such as non-modified (selenium free) ruthenium nano-particles or the bare carbon support were studied by ASAXS. The scattering curves were taken at 5 energies for that the anomalous scattering amplitude f' , varies equidistant in the vicinity below the selenium and the ruthenium K absorption edges, respectively. We took special care to extend the q -range up to larger values, according to get structural information also from sub nanometer structures.

Fig. 3 left shows that Ru and Se form nano-structures that alter the shape of the Black Pearls scattering curve dramatically. The sample which contains Selenium (Fig. 3 right) shows a small hump at $Q \sim 7 \text{ nm}^{-1}$ that is visible also at the Ru-K edge (Fig. 3 left). It was deduced that selenium within the sample generates clearly detectable and analyzable sub nanometer sized structural features.

Taken into account the energy dependences (the anomalous dispersion effect in the vicinity of the Se- and the Ru-edge as well) of the scattering intensity of all measured samples, a structure model of the catalytically active metallic nano-particles has been deduced, suggesting a nearly spherical Ru particles with mean diameters of 2.3 nm decorated with Se aggregates. These structures onto the ruthenium nano-crystallites feature a diameter less than 0.6 nm. These results are supported by data from XRD and EXAFS measurements, obtained from the same materials [3, 4]. Even so, the real shape of these of only few atoms consisting selenium clusters is not yet finally clarified. However, it is suggested to represent a symmetric ring like observed for free selenium clusters [5].

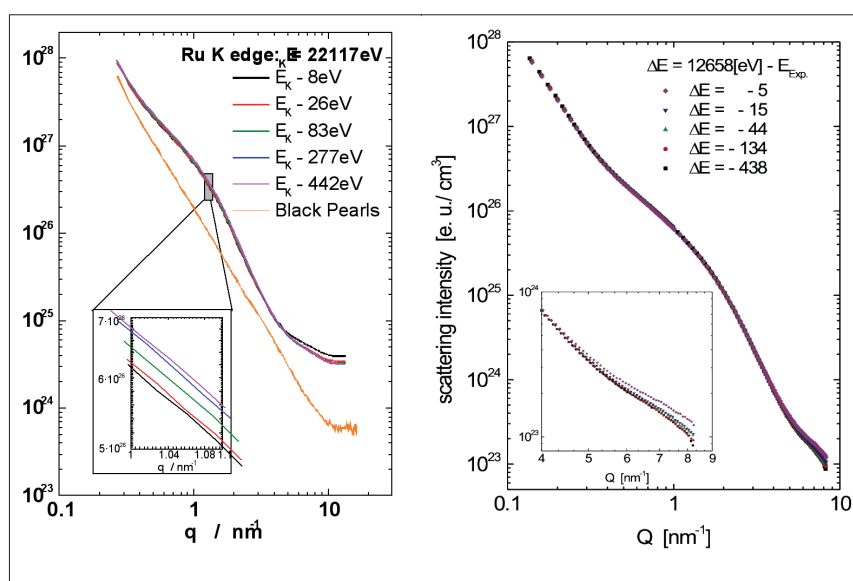


Fig. 3: The ASAXS curves measured near below the K-absorption edges of ruthenium (left) and selenium (right) allowed to distinguish three structural elements.

We also confirmed by ASAXS that the selenium modification renders the ruthenium nano-particles extremely resistant against agglomeration and particle growth. The average particle size of the ruthenium particles was found to remain below 2.5 nm in diameter even after long annealing at 800°C.

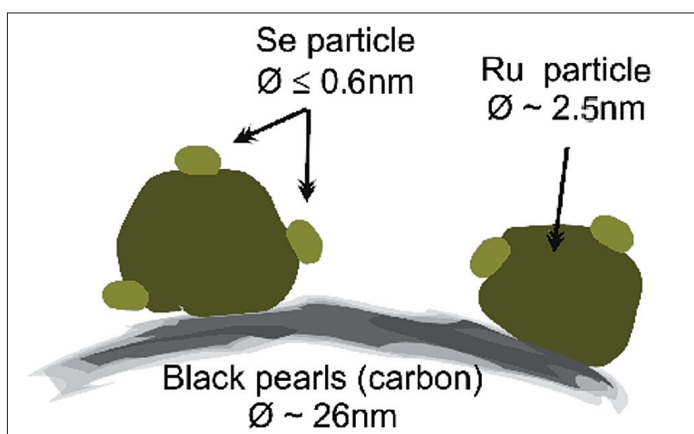


Fig. 4: Suggested scattering equivalent structural model for ruthenium based electrocatalysts supported on activated carbon and modified with selenium.

- [1] Alonso-Vante, N.; Bogdanoff, P.; Tributsch, H.: On the Origin of the Selectivity of Oxygen Reduction of Ruthenium - Containing Electrocatalysts in Methanol - Containing Electrolyte; *J. Catalysis* **190** (2000) 240.
- [2] U. Paulus, PhD-Thesis, ETH Zürich, 2002.
- [3] Fiechter, S.; Dorbandt, I.; Bogdanoff, P.; Zehl, G.; Schulenburg, H.; Tributsch, H.; Bron, M.; Radnik, J.; Fieber-Erdmann, M.: Surface modified Ruthenium nanoparticles: structural investigation and surface analysis of a novel catalyst for oxygen reduction; *Journal of Physical Chemistry C* **111** (2007) 477-487.
- [4] Zehl, G.; Dorbandt, I.; Fiechter, S.; Bogdanoff, P.: On the Influence of Preparation Parameters on the Catalytic Properties of Carbon Supported Ru-Se Electrocatalysts; *Journal of New Materials for Electrochemical Systems*, submitted.
- [5] Becker, J.; Rademann, K.; Hensel, F.: Ultra-violet photoelectron studies of the molecules Se_5 , Se_6 , Se_7 and Se_8 with relevance to their geometrical structure; *Z. Phys. D. - Atoms, Molecules and Clusters* **19** (1991) 229.

Corresponding author:

S. Fiechter
fiechter@hmi.de

Novel approaches to quasi solid state electrolytes in dye sensitized solar cells

M. Junghänel and H. Tributsch

■ HMI, SE5

Introduction

Dye sensitized solar cells (DSC, Fig.1) have attracted significant attention over the last decade [1-3] and appear to be close to enter the market. A wide bandgap semiconductor (TiO_2) is sensitized with an organic dye molecule (most often Ru-complexes) yielding conversion efficiencies of 10,4 % [4]. Since the cell concept is based on the transport of majority charge carriers, the purity of the materials is less important compared to conventional Si solar cells making the device potentially very cheap. Though intrinsic stability has been proven [5] in several studies, the employment of a liquid electrolyte demands a hermetic sealing for at least 20 years which is an unsolved problem so far. At HMI the nano surface conductivity solar cell (NSCSC) is developed that is based on a quasi solid state electrolyte which is in equilibrium with the ambient atmosphere making an extra sealing redundant.

Preparation of nano surface conductivity solar cell

The preparation is based on low-cost techniques and materials trying to make the cell assembly as simple as possible. On a F:SnO_2 coated glass (sheet resistance $10 \Omega/\square$) a $10 \mu\text{m}$ thick layer of nanoporous TiO_2 particles (diameter 20 nm) is screen printed. The electrode is stained by dipping it into a 0,5 mM dye solution of a Ru-bipyridil-complex (s. Fig 1).

On top a layer of carbon particles is deposited by doctor blading that acts both as a rectifying contact and as a catalyst for electron regeneration. It replaces the expensive noble metal platinum that is employed in classical DSC. Finally the TiO_2 surface is covered with lithiumiodide (LiI) by dip coating. Any remaining solvent is removed under reduced pressure (10^{-6} mbar for 2 hours). After equilibration with the ambient atmosphere the hygroscopic LiI is partly hydrated. It is proposed that by partial oxidation of iodide long poly iodide chains are formed that allow charge transport by a Grotthuss-type mechanism. A cross section SEM picture is shown in Fig. 2.

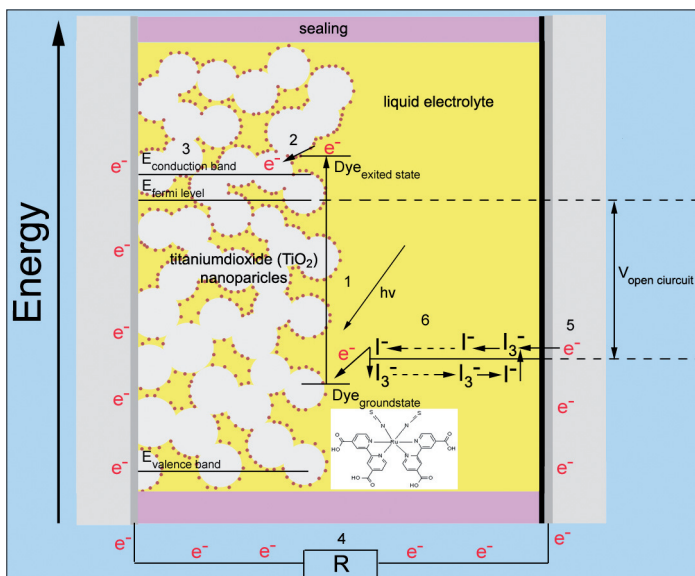


Fig. 1: operation principle of a dye sensitized solar cell

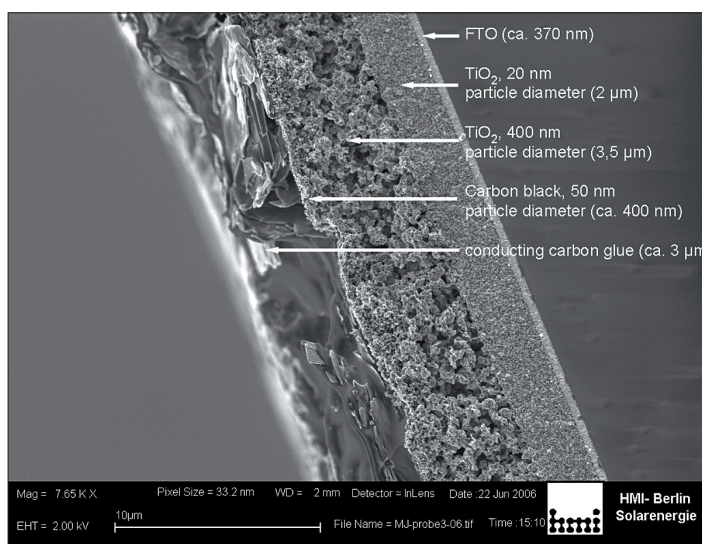


Fig. 2: SEM cross section of a nano surface conductivity solar cell

Thermogravimetric analysis (TGA)

Iodine with a vapor pressure of 0,41 hPa at RT might be susceptible to evaporation if it is not chemically bound. TGA-MS analysis revealed that up to 80 °C no iodine desorbs from the surface making cell operation without sealing possible even at higher temperature (Fig. 3). However, water reversibly desorbs from the surface for temperature >40 °C, lowering the conductivity of the LiI/I-film and thus limiting the photocurrent. The best performance is achieved for temperatures between 35-40 °C.

Cell efficiency and outlook

The cell parameters of an average NSCSC cell are $I_{SC} = 3,4 \text{ mAcm}^{-2}$, $V_{OC} = 635 \text{ mV}$, efficiency = 1,1 %. The cell efficiency is limited by an insufficient current collection. Photovoltage transient measurements revealed that there is a significant charge transfer resistance between the TiO_2 nanoparticles on the FTO working electrode. It is the main challenge to lower this energy barrier and enhance charge extraction.

The recombination rate between conduction band electrons and electron acceptors on the TiO_2 surface is already comparable to conventional DSC. At 1 sun the electron lifetime is between 2-4 ms. Current research focuses on the long term stability of the device and a better understanding of the hole transport mechanism.

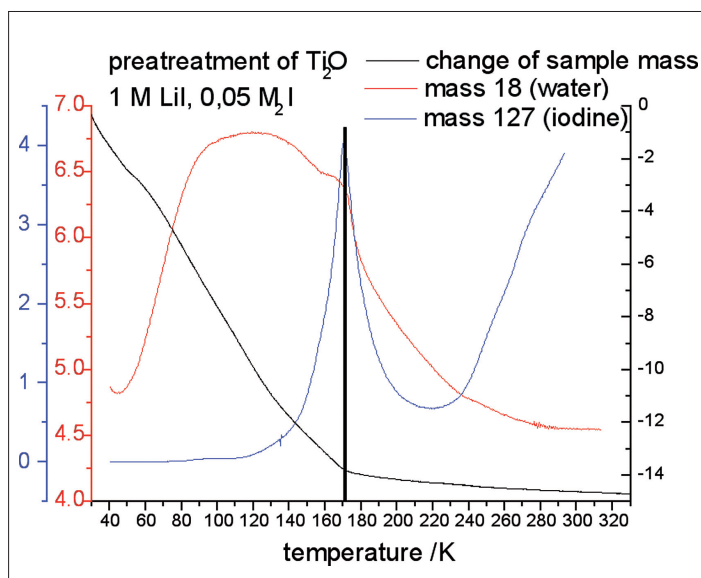


Fig. 3: Thermogravimetric analysis (TGA) of nano surface conductivity solar cell

- [1] H. Tributsch, Photochem. Photobiol. **14**, 95 (1971)
- [2] B. O'Regan, M. Grätzel, Nature **353**, 737-739 (1991)
- [3] M. Junghänel, H. Tributsch, J. Phys. Chem. B **109**, 22876-22883 (2005)
- [4] M. A. Green, K. Emery, D. L. King, Y. Hishikawa, W. Warta, Prog. Photovolt: Res. Appl. **14**, 455-461 (2006)
- [5] P. Wang, C. Klein, R. Humphrey-Baker, S. Zakeeruddin, M. Grätzel, Applied Physics Letters **86**, 123508 (2005)

Nanostructured Injection Solar Cell with Tungsten Disulfide Absorber

M. Thomalla, H. Tributsch

■ HMI, SE5

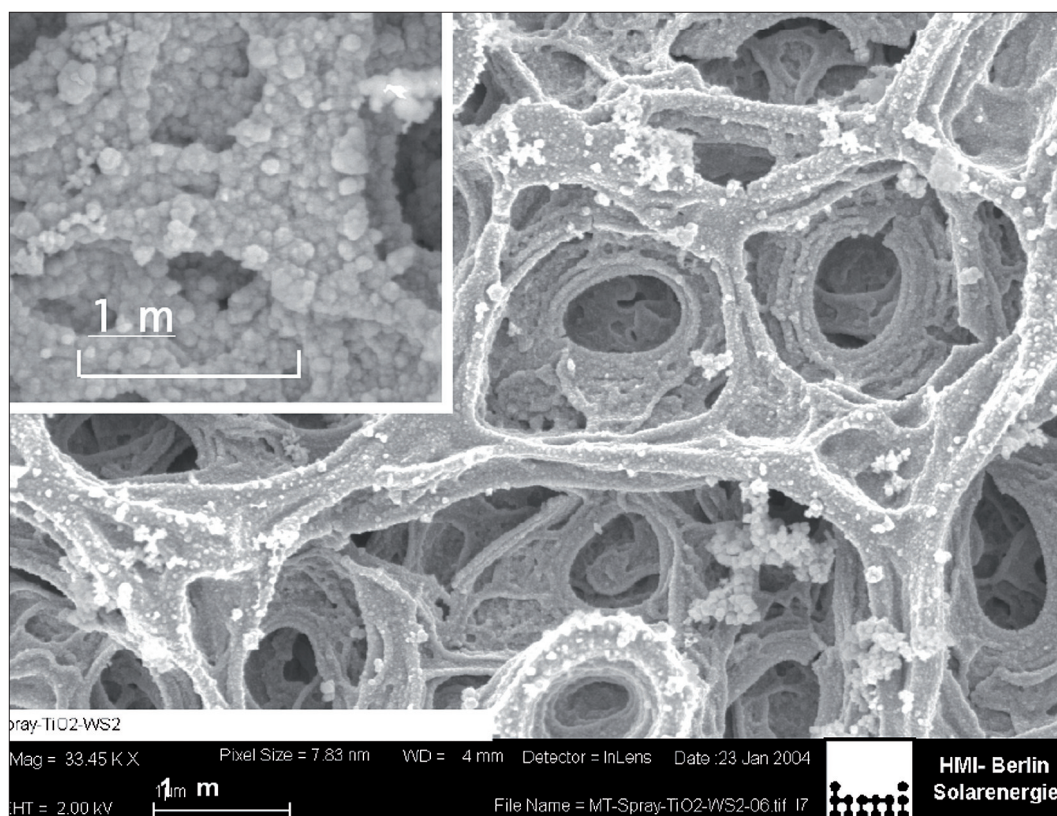


Fig. 1: TiO₂ substrate spray pyrolysis

Nanostructured photoelectrochemical solar cells have received considerable attention in recent years as an alternative to conventional solar cells. In particular, the solar cell developed by Grätzel and his group with its high solar energy conversion of up to 11% has increased the research efforts in this field. Unfortunately the original $\text{cis-RuL}_2(\text{SCN})_2$ with $\text{L} = 2,2'$ -bipyridyl-4,4'-dicarboxylatoacid (bpca) dye has not the desirable stability of 20 years [2,3,4,5] and in addition the chemical stability of the iodine redox system, the volatility of the solvent and the sealing of the cells remain unsolved. An interesting approach is to replace the organic dye with an inorganic semiconductor quantum dot. Semiconductor quantum dots have several advantages. Firstly, their band gap can be easily adjusted by changing the

size of the particle to match the solar spectrum and the band gap of TiO₂. Secondly, they may be selected to possess a high absorption coefficient, which allows to produce very thin absorber and to reduce the amount of materials needed. And most important, it may be possible to apply a metallically conducting nano-contact as they are used in traditional solid states solar cells.

Porous, nanostructured sol gel - TiO₂ (100 nm) has been sensitized with WS₂ quantum sheets (~5 nm) with the help of chemical bath deposition (CBD has been chosen out of several deposition methods which have been tested, e.g. electrochemical bath deposition, inverse micelles, sputtering, nanotubes). The absorber has been characterized with help of EDX, TEM, SEM, Ra-

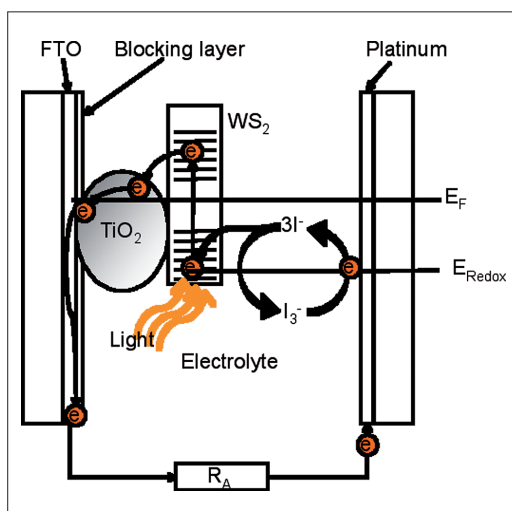


Fig. 2: Schematic presentation of $\text{TiO}_2\text{-WS}_2$ injection solar cell

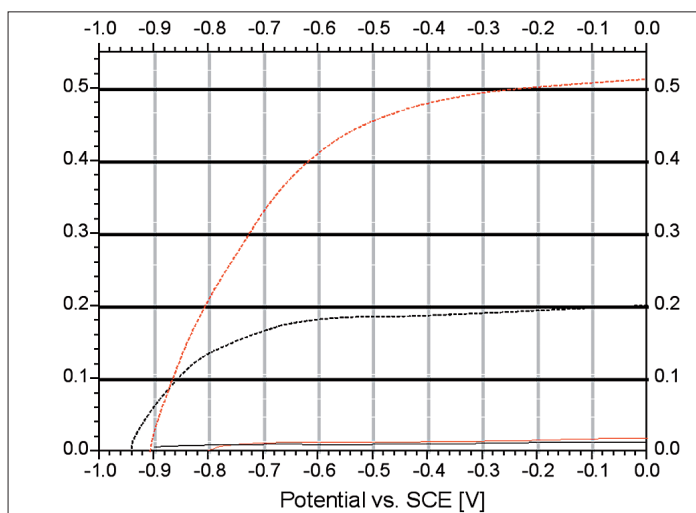


Fig. 3: I - U curve of a sensitization solar cell before (black curve) and after (red curve) of the $\text{TiO}_2\text{-WS}_2$ electrode with cystein

man spectroscopy and light absorption measurements. The photosensitization was confirmed via electrochemical measurements. The surface of TiO_2 has been modified by a thin Al_2O_3 film, which significantly enhanced the photocurrent density to $0.4\text{-}0.7\text{ mA/cm}^2$.

The TiO_2 layers which serve as substrates for the absorber had to be optimized. The best and stable substrates were produced with sol gel method and spray pyrolysis (Fig. 1). The geometry of the cell is shown in Fig. 2.

Treating the electrode with various chemicals e.g. cysteine, which is well known as electron transfer molecule in biological system, increased the photocurrent significantly, as can be seen in Fig. 3. It is suggested that cysteine can on the one hand passivate the dangling bonds of the WS_2 nano sheets and therefore decrease recombination processes. On the other hand due to its unique electronic structure and the ability to conduct electrons in only one direction it could serve as a bridge between the electrolyte and the absorber increasing the photocurrent.

- [1] B. O'Reagan, M. Grätzel, *Nature* **353** (1991) 737
- [2] H. Greijer Agrell, J. Lindgren, A. Hagfeldt *Solar Energy*, **75** (2003), 169-180
- [3] M. Turrion, B. Macht, P. Salvador, H. Tributsch, *Z. Phys. Chem.* **212** (1999) 51
- [4] B. Macht, M. Turrion, A. Barkschat, P. Salvador, K. Elmer, H. Tributsch, *Solar Energy Mater. Solar Cells* **73** (2002) 163
- [5] M. Thomalla, H. Tributsch, *J. Phys. Chem. B.*; 2006, 110, 12167-12171.

Epitaxial SiC-ZnO interfaces, electronics and morphology

S. Andres, T. Seyller, C. Pettenkofer

■ HMI, SE6

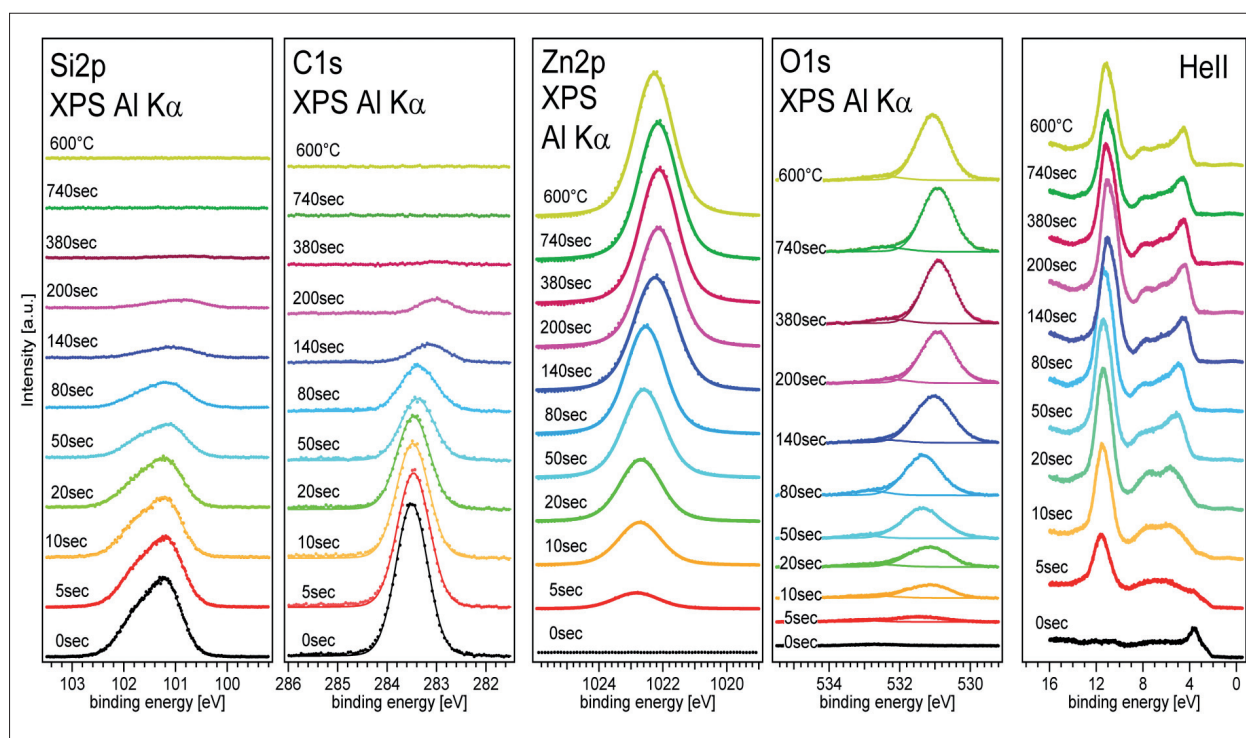


Fig. 1: Valence and Corelevel spectra in the course of ZnO deposition on (0001) 6H SiC

Transparent electronics are a hot topic in today's material research. We report here on the fabrication and surface characterization of a simple heterostructure made from the wide band gap materials ZnO and 6H-SiC. Due to the necessary wide band gap needed for the contact partners in a transparent diode, doping and interface properties play a crucial role in the process of contact formation.

n-type 6H-SiC (0001) surfaces were hydrogen terminated [2,3] and found to be free of oxide and hydrocarbon contaminations on a sub monolayer level. ZnO is deposited by a specifically developed MOMBE technique [1]. All preparation and analysis steps were performed in a true ultra high vacuum environment to ensure a contamination free investigation of the device during all steps of the fabrication. The electronic structure of the interface is monitored by surface sensitive

electronspectroscopies like UPS and MXPS (Ultraviolet and Monochromatic X-ray Photoelectron Spectroscopy).

Substrate and film core level and valence band spectra (Fig.1) show nicely the layer by layer growth of a clean and non-reactive abrupt ZnO

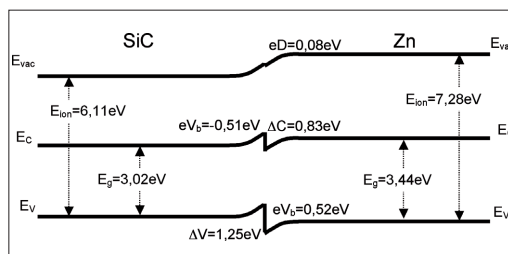


Fig. 2: Band alignment of the SiC-ZnO heterojunction as derived from the data displayed in Fig. 1

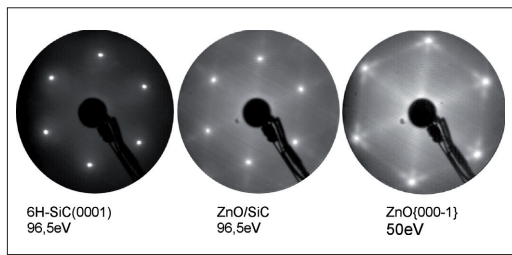


Fig. 3: LEED pattern for the substrate, film and at different energy showing the facets of the Zn-terminated surface

interface on the SiC substrate. Which means no chemical intermixing between the contact partners takes place. LEED data proof the crystallinity and order of the growing (0001) ZnO film forming a diode device. From Fig 1 the band alignment of the diode may be derived as shown in Fig 2.

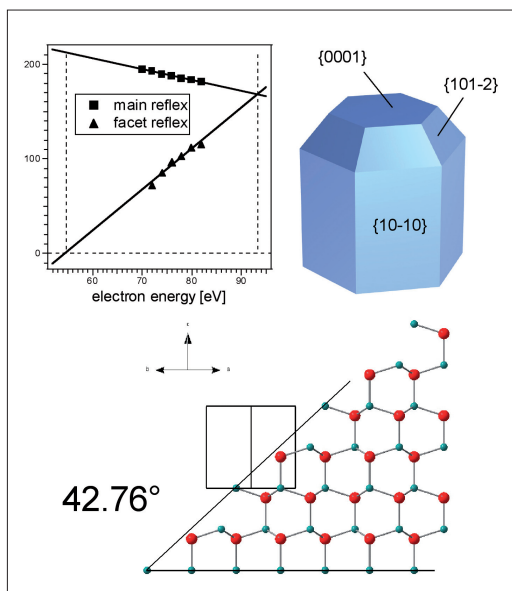


Fig. 4: Evaluation of the facet type from the LEED data for the epitaxial (0001) ZnO surface

The data reveal the band bending in the substrate and film as a consequence of the charge carrier distributions in the interface region, given by the doping of the film and the substrate. The band offsets e.g. the difference of the valence band edges for both contact phases are given by the local atomic and electronic structure direct at the contact plane. The specific atomic arrangement and the electronic states present at a particular surface determine the offsets, which by itself determine the functionality of the device.

Here we see the unusual case that no resulting interphase dipole is detected as to be seen as a nearly smooth transition in the vacuum level from SiC to ZnO. Often a dipolar contribution in the order of 1eV is detected in heterodiodes influencing the band alignment. The missing interface dipole gives the opportunity to vary the band alignment in the band offsets according to the needs of a particular device by introducing bond modifications in the contact plane. As our LEED-data proof, the oxygen termination of the (0001) ZnO surface forms the interface to the SiC surface. A modification by the introduction of a specifically designed interfacial layer is a promising perspective to tailor the electric properties of the diode. The morphology of the prepared diode is derived from the LEED data.

The ZnO film grows epitaxial in a layer by layer growth mode with a faceting of the ZnO surface which is indicative for a Zn termination of the vacuum interface of the film. Consequently an oxygen termination has to be present for this polar crystal surface at the SiC-ZnO interface. The evaluation of the facet is given in Fig 3. The behavior of the LEED spots responsible for the (000-1) surface with respect to the facet signals is plotted against the electron energy. The obtained angle of 43° is in good agreement to the proposed (101-2) facet, which is appearing due to the lower energy needed to build a non polar surface with respect to the purely Zn-terminated (000-1) surface. This evaluation is shown in Fig 4.

This example shows nicely the power of surface analytical tools in the characterization of the morphology and electronic properties of a proposed device. Even the perspectives of a future improvement of the device can be deduced from the obtained data. Future work will be directed to variations in the doping of the SiC substrate, as a p-doped SiC for our first investigations was not available. Further attempts will be made to grow p-type ZnO layer.

- [1] Andres A.; Pettenkofer C.: Epitaxial deposition of ZnO. In: Ellmer K. ; Stadermann G. [Eds.] : TCO für Dünnschichtszell- und andere Anwendungen III : Workshop 10. - 12.04.2005 in Freyburg / Unstrut. Berlin: Forschungsverbund Sonnenenergie c/o Hahn-Meitner-Institut, 2005 p.25-27
- [2] T. Seyller, J. Phys.: Condens. Matter **16**, S1755 2004
- [3] N. Sieber, B. F. Mantel, T. Seyller, J. Ristein, L. Ley, T. Heller, D. R. Batchelor, and D. Schmeißer, Appl. Phys. Lett. **78**, 1216 2001.